UNIVERSITY OF OKLAHOMA

GRADUATE COLLEGE

Nearfield Beamforming of a Multi-Input Multi-Output Radar System

A THESIS

SUBMITTED TO THE GRADUATE FACULTY

in partial fulfillment of the requirements for the

Degree of

MASTER OF SCIENCE

By

Ryan Jones
Norman, Oklahoma
2026

Nearfield Beamforming of a Multi-Input Multi-Output Radar System

A THESIS APPROVED FOR THE
SCHOOL OF ELECTRICAL AND COMPUTER ENGINEERING

BY THE COMMITTEE CONSISTING OF

Dr. Yan Zhang, Chair

Dr. Nathan Goodman

Dr. Tian-You Yu

Acknowledgments

I would like to express my gratitude to Dr. Yan (Rockee) Zhang, my advisor, for invaluable guidance and mentorship throughout this work. My sincere thanks to Dr. Nathan Goodman, whose Radar imaging course taught me the fundamental elements implemented in the simulation used in this research. I am thankful to Dr. Jessica Ruyle for her instruction in antenna fundamentals and computational electromagnetics. I'd like to thank my committee members for their support and patient instruction. Finally, I would like to thank Melody Metivier Jones, my wife, for her tremendous sacrifice of time and energy to support this endeavor.

Contents

List Of Tables **vii**

List Of Figures **viii**

Abstract **x**

1 Introduction **1**
- 1.1 Background of Radar Systems . . . 1
- 1.2 MIMO Radar Applications . . . 2
- 1.3 Challenges of MIMO Nearfield Beamforming and Target Detection . . 3
- 1.4 Thesis Outline . . . 4

2 Description of the MIMO Array **5**
- 2.1 Background . . . 5
- 2.2 Minimum Redundancy Array . . . 6
- 2.3 Antenna Modeling . . . 6
  - 2.3.1 Dipole . . . 6
  - 2.3.2 Patch . . . 10

3 Beamforming Algorithms **12**
- 3.1 Far Field Beamforming . . . 12
- 3.2 Nearfield Beamforming . . . 13

4 Description of MIMO Radar System Simulation **16**
- 4.1 Code Structure . . . 16
- 4.2 Waveform Generation . . . 17
- 4.3 Waveform Propagation Environment . . . 19
  - 4.3.1 MIMO Lattice . . . 19
  - 4.3.2 Mutual Coupling . . . 19
  - 4.3.3 Target Definition . . . 21
- 4.4 Receiver . . . 23
- 4.5 Matched Filter . . . 23
- 4.6 Beamforming . . . 24
- 4.7 Range-Doppler Processing . . . 26
- 4.8 Target Detection . . . 26

5 Results and Data Analysis **28**
5.1 Range-Azimuth Processing . . . 28
5.2 Range-Doppler Processing . . . 36
5.3 Spherical Beamforming . . . 39
5.4 Sidelobe Levels . . . 42

6 Conclusion and Future Work **49**
6.1 Summary of Contributions . . . 49
6.2 Future Work . . . 49

References **52**

Appendix A - List Of Symbols **55**

Appendix B - List Of Acronyms and Abbreviations **58**

List Of Tables

5.1 Moving target parameters 36
5.2 Summary of sidelobe level improvement in decibels of spherical beamforming over planar beamforming 48

List Of Figures

1.1 Simple Radar block diagram 2

2.1 MIMO Lattice 6

2.2 Far-field gain of a half-wavelength dipole antenna located at the origin with wires running parallel to the z-axis vs. the polar angle 10

2.3 10 GHz patch antenna modeled in HFSS 11

2.4 Error between the gain calculated from near-field values and the far-field gain 11

3.1 Far-field Beamforming 13

3.2 Near-field Beamforming 15

4.1 Simulation Code Structure 17

5.1 Spherical coordinate system used to define scatterer locations. r' is the radial distance from the phase center of the virtual array to the scatterer and the z-axis is the polar axis. All array elements are arranged along the y-axis and half-wavelength dipoles are aligned with the z-axis. 29

5.2 Range-azimuth maps showing the stages of threshold detection using 15 scatterers spaced 4 meters apart along $\phi' = 0^\circ$ and $\theta' = 90^\circ$ processed with planar beamforming on a MIMO dipole lattice 31

5.3 Range-azimuth maps showing the stages of threshold detection using 15 scatterers spaced 4 meters apart along $\phi' = 0^\circ$ and $\theta' = 90^\circ$ processed with planar beamforming on a MIMO dipole lattice without mutual coupling 32

5.4 Range-azimuth maps showing the stages of threshold detection using 15 scatterers spaced 4 meters apart along 0° azimuth and processed with planar beamforming on a MIMO patch lattice 33

5.5 Range-azimuth maps showing the stages of threshold detection using 15 scatterers spaced 4 meters apart along 0° azimuth and processed with planar beamforming with a high noise floor 35

5.6 Range-azimuth maps showing the stages of threshold detection with scatterers arranged according to Table 5.1 and processed with planar beamforming 37

5.7 Range-Doppler maps showing the stages of threshold detection with scatterers arranged according to Table 5.1 and processed with planar beamforming 38

5.8 Range-azimuth maps showing the stages of threshold detection using 15 scatterers spaced 4 meters apart along 0° azimuth and processed with spherical beamforming 39
5.9 Range-azimuth maps showing the stages of threshold detection with scatterers arranged according to Table 5.1 and processed with spherical beamforming 40
5.10 Range-Doppler maps showing the stages of threshold detection with scatterers arranged according to Table 5.1 and processed with spherical beamforming 41
5.11 Comparison of integrated and peak sidelobe levels between planar and spherical beamforming methods for scatterers positioned along 0° azimuth and positioned every 4 meters starting at 1 meter. 43
5.12 Comparison of power magnitude vs. azimuth for range bins $r = 1$ meter and $r = 57$ meters using planar and spherical beamforming methods with targets along the $\phi' = 0^\circ$ look angle. 44
5.13 Comparison of planar and spherical beamforming methods using 15 targets spaced 4 meters apart along 5° azimuth 45
5.14 Comparison of planar and spherical beamforming methods using 15 targets spaced 4 meters apart along -25° azimuth 46
5.15 Comparison of power magnitude vs. azimuth for range bins $r = 1$ meter and $r = 57$ meters using planar and spherical beamforming methods with targets along the $\phi' = 5^\circ$ look angle. 47
5.16 Comparison of power magnitude vs. azimuth for range bins $r = 1$ meter and $r = 57$ meters using planar and spherical beamforming methods with targets along the $\phi' = -25^\circ$ look angle. 47

Abstract

As multi-input multi-output (MIMO) radars become essential for reducing the number of active channels and the overall size, weight, and power (SWaP) of future radars, interest in applying MIMO radar techniques to real-world missions has increased. One challenge that is not fully understood is the near-field effect of MIMO virtual arrays, which is relevant for systems with either a large array or aperture size, relatively long operating wavelengths, or short-range target distances. In this study, we first developed a Python-based, open-source simulation tool that models basic range-dependent effects in MIMO beamforming and supports the incorporation of more realistic antenna patterns. From there, we analyzed the signatures of multiple moving point targets based on simple time-multiplexing transmit MIMO in the array field-of-view, with different speeds and arrival angles, from far field to near field ranges, to derive quantitative relationships that connect the system parameters and antenna performance to the signature sidelobe levels and the angle estimation accuracy. Based on this analysis and data, an algorithm that applies a novel beamforming approach that leverages both range dependence and near-field radiation-pattern compensation to accomplish near-field target detection and location. The effectiveness of the proposed approach is validated through analytical modeling and various simulations using Python-based system simulation tools.

Chapter 1

Introduction

1.1 Background of Radar Systems

Radar sensors are used in autonomous navigation systems to measure the surrounding environment under various weather conditions. Other solutions utilizing LiDAR and cameras may offer higher visual fidelity under ideal conditions, but rain, darkness, fog, sea spray, and airborne particles such as dust significantly degrade their performance. Radar also provides reliable range measurements that remain consistent in the presence of clutter and dynamic sea conditions. Modern camera systems can estimate motion or depth using stereo vision, but still rely on stable lighting and clear visibility. In the ocean, those conditions are not guaranteed. Together, these characteristics motivate the use of radar as the primary sensor throughout this thesis.

This work examines, through simulation and analysis, the synthesis of a Radar system. The basic elements of a radar system include a waveform generator, transmitter, an antenna or antennas, a receiver, and some kind of signal processing. The waveform generator is responsible for producing the electromagnetic properties desired for the radar operation. That may include frequency, phase, and amplitude modulation as well as any signal mixing to achieve the desired transmit frequency. The transmitter amplifies the generated waveform, giving it sufficient power to produce detectable echoes in the propagation environment. The antenna or antennas provide additional signal gain by focusing the radiated energy and performing spatial filtering to achieve direction-finding. The receiver amplifies the faint signal echoes from scatterers in the propagation environment, and the signal processor synthesizes those echoes into meaningful information for the radar operator. Fig. 1.1 shows a simplified block diagram of a generic radar system. This thesis will describe the operation of each element of the radar system and how to model them and integrate their models into a cohesive radar system simulation.

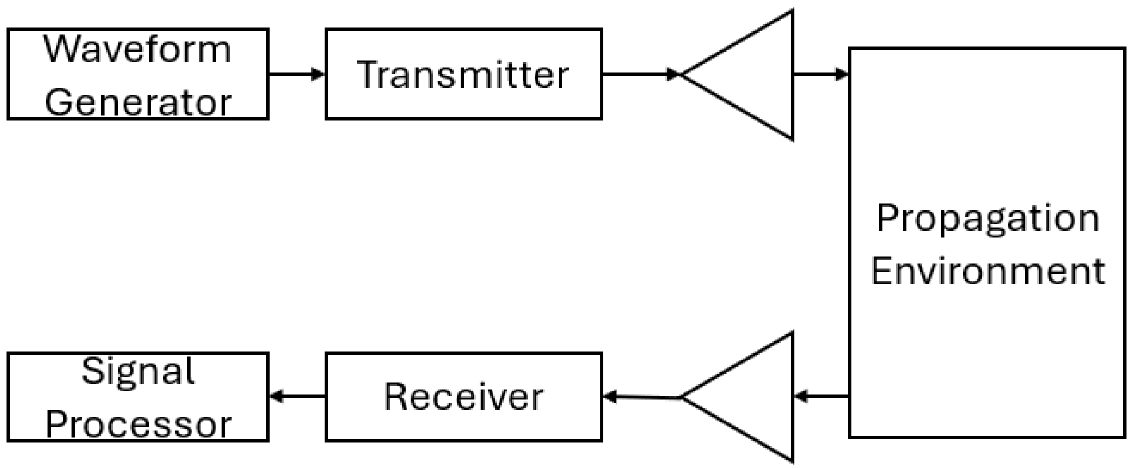

Figure 1.1: Simple Radar block diagram

1.2 MIMO Radar Applications

MIMO arrays and signal processing will be an important trend in future low-cost, low SWaP radar sensor designs for the UxV (unmanned vehicle) platforms [1–4]. These arrays rely on phase differences among the antenna elements to form a highly directional beam pattern, similar to that of a typical phased array. The difference between MIMO and a typical phased array is that each transmit antenna in the array produces an independent signal, uncorrelated with the others. This has the advantage of yielding a consistent average Radar cross-section (RCS) when detecting scintillating scatterers [5]. MIMO also produces a virtual array with a larger aperture than the physical array, yielding greater directivity in signal reception and finer angular resolution for target localization and image formation [3]. The disadvantage of MIMO radar is increased complexity in signal generation and processing, and greatly reduced directivity in signal transmission compared to a conventional phased array [6]. The orthogonality of MIMO signals can provide many degrees of freedom for adaptive beamforming techniques, such as space-time adaptive processing (STAP), to mitigate clutter in automotive ground moving-target indicator radar [7].

1.3 Challenges of MIMO Nearfield Beamforming and Target Detection

The scenarios that require MIMO array radars to operate in the near-field zones may occur under two conditions: a large, massive MIMO structure at long range [8, 9], and a small MIMO array aperture that needs to focus at very close ranges [10, 11] for collision avoidance, security imaging [12], or medical scanning [13]. In both cases, the traditional planar-wave assumption for beamforming would no longer be accurate, while the spherical-wavefront-based beamformer for a MIMO array has not been fully studied before. This thesis intends to fill the gap by investigating the key beamforming and processing performance of a generic MIMO radar sensor that uses a specific Minimal Redundancy Array (MRA) design and a Python-based end-to-end pulsed radar simulator. Prior work in the area of MIMO radar operation on near targets is related to Synthetic Aperture Radar imaging techniques. The contribution of this thesis is an algorithm for detecting and locating close-range hard targets and a system simulation to investigate its effectiveness.

1.4 Thesis Outline

The rest of this thesis is organized as follows: Chapter 2 will describe the MIMO lattice studied in this thesis, including the arrangement of the MIMO antenna elements and how the elements are modeled in the simulation. Chapter 3 will describe beamforming with a MIMO array and a beamforming method for near-field target detection. Chapter 4 will provide a detailed description of the simulation environment, including the waveform generator, transmitter, MIMO array, propagation environment, receiver, and processing algorithms. Chapter 5 presents the data results and an analysis of the simulations for various target environments. Conclusions and future work will be provided in Chapter 6.

Chapter 2

Description of the MIMO Array

2.1 Background

MIMO arrays are a mature and widely implemented technology for wireless communications applications. The flexibility to leverage beamforming and signal orthogonality provides advantages in data throughput and signal coverage.

More recently, there is a growing interest in MIMO arrays for Radar applications. The primary advantage MIMO provides Radar is the ability to form a virtual antenna array that has a larger aperture than the size of the physical array. Depending on the lattice arrangement, the virtual array can be nearly double the size of the physical array. Since beamwidth is proportionate to aperture size, this means higher gain and improved signal resolution. The tradeoff is that a MIMO array does not form a coherent transmit beam the way a phased array does. All beamforming occurs in the receiver. So while angular resolution may be improved over a phased array of similar size, the maximum detection range as a function of transmit power is significantly less.

MIMO arrays tend to produce virtual arrays with redundant elements. In order to form a coherent beam, these redundant elements must be amplitude-weighted, further reducing the efficiency of the array.

2.2 Minimum Redundancy Array

The MIMO lattice studied in this work is the Minimum Redundancy Array from Kim [14] modified so that each subarray only has one element. Fig. 2.1 shows the arrangement of the transmit and receive elements as well as the virtual array they produce.

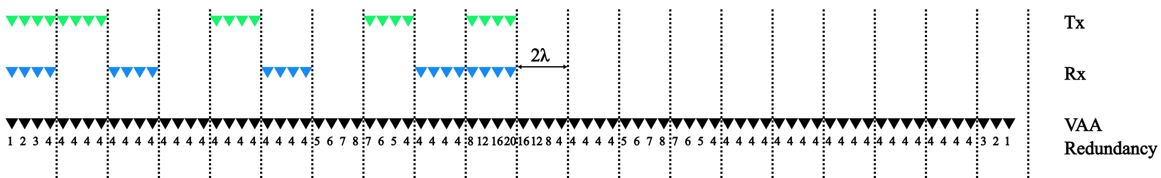

Figure 2.1: MIMO Lattice

2.3 Antenna Modeling

2.3.1 Dipole

Most of the results discussed in this paper will be derived for the half-wavelength dipole, as closed-form models already exist for its radiation characteristics, self-impedance, and mutual impedance [15]. Although this thesis uses the term "nearfield" to describe the spherical beamforming method, the nearest target in every simulation is over 33λ from the phase center of the array, placing it in the far-field region when discussing dipole radiation characteristics. At 1 meter, a target is close enough to the array to cause significant phase errors for planar beamforming method, but is too far to be in the Fresnel or reactive nearfield regions of individual antenna elements. To derive the far-field gain of the half-wavelength dipole, we will start with the radiation characteristics of an infinitesimal dipole centered at the origin and aligned parallel to the z-axis:

$$E_r = \eta \frac{kI_0 l \sin\theta}{4\pi r^2} \left[1 + \frac{1}{jkr}\right] e^{-jkr} \tag{2.1a}$$

$$E_\theta = j\eta \frac{kI_0 l \sin\theta}{4\pi r} \left[1 + \frac{1}{jkr} - \frac{1}{(kr)^2}\right] e^{-jkr} \tag{2.1b}$$

$$E_\phi = 0 \tag{2.1c}$$

$$H_r = 0 \tag{2.1d}$$

$$H_\theta = 0 \tag{2.1e}$$

$$H_\phi = j \frac{kI_0 l \sin\theta}{4\pi r} \left[1 + \frac{1}{jkr}\right] e^{-jkr}. \tag{2.1f}$$

E_r, E_θ, and E_ϕ in Eq. 2.1 are the radial, polar, and azimuthal components of the electric field, respectively. H_r, H_θ, and H_ϕ in Eq. 2.1 are the radial, polar, and azimuthal components of the magnetic field, respectively. $k = 2\pi/\lambda$ is the wavenumber, r is the distance from the origin, I_0 is the current on the dipole, and l is the length of the dipole. These radiation characteristics rely on an evenly distributed current along the dipole, which vanishes at the ends; this assumption is only valid for dipoles much shorter than the signal wavelength.

In the far-field radiation region defined as distances from the dipole $kr >> 1$ the radiation characteristics can be estimated by dropping the terms in Eq. 2.1 related to $1/r^2$ and $1/r^3$ to become:

$$E_r \simeq 0 \tag{2.2a}$$

$$E_\theta \simeq j\eta \frac{kI_0 l \sin\theta}{4\pi r} e^{-jkr} \tag{2.2b}$$

$$E_\phi = 0 \tag{2.2c}$$

$$H_r = 0 \tag{2.2d}$$

$$H_\theta = 0 \tag{2.2e}$$

$$H_\phi \simeq j \frac{kI_0 l \sin\theta}{4\pi r} e^{-jkr} \tag{2.2f}$$

A very thin finite length dipole has current distribution of

$$\mathbf{I_e}(x', y', z') = \left\{ \begin{array}{lll} \mathbf{\hat{a}_z} I_0 \left[k \left(\frac{1}{2} - z' \right) \right] & for & 0 \leq z' \leq l/2 \\ \mathbf{\hat{a}_z} I_0 \left[k \left(\frac{1}{2} + z' \right) \right] & for & -l/2 \leq z' \end{array} \right\} \tag{2.3}$$

so that Eq. 2.2b becomes

$$\begin{aligned} E_\theta \simeq j\eta \frac{kI_0 e^{-jkr}}{4\pi r} \sin\theta \Bigg\{ \int_{l/2}^{0} \sin\left[lwf[k \left(\frac{l}{2} + z' \right) \right] e^{jkz' \cos\theta} dz' \ldots \\ + \int_{l/2}^{0} \sin\left[lwf[k \left(\frac{l}{2} - z' \right) \right] e^{jkz' \cos\theta} dz' \Bigg\} \end{aligned} \tag{2.4}$$

which reduces to

$$E_\theta \simeq j\eta \frac{I_0 e^{-jkr}}{2\pi r} \left[\frac{\cos\left(\frac{kl}{2} \cos\theta \right) - \cos\left(\frac{kl}{2} \right)}{\sin\theta} \right] \tag{2.5}$$

for a finite-length dipole observed from the far field. Using the far field relation $E_\theta \simeq H_\phi \eta$ the ϕ component of the magnetic field of a finite length dipole is

$$H_\phi \simeq j \frac{I_0 e^{-jkr}}{2\pi r} \left[\frac{\cos\left(\frac{kl}{2} \cos\theta \right) - \cos\left(\frac{kl}{2} \right)}{\sin\theta} \right] \tag{2.6}$$

Antenna gain can be defined as

$$G(\theta, \phi) = e_{cd} \left[4\pi \frac{U(\theta, \phi)}{P_{rad}} \right] \tag{2.7}$$

where e_{cd} is the combined conductive and dielectric efficiency of the antenna, P_{rad} is the radiated power from the antenna, and $U(\theta, \phi)$ is the radiation intensity from the antenna in a given direction [15] defined as

$$U = r^2 W_{av}. \tag{2.8}$$

W_{av} is the magnitude of the average power density vector related to the electric and magnetic field vectors by

$$\mathbf{W_{av}} = \frac{1}{2} \Re[\mathbf{E} \times \mathbf{H}^*] \tag{2.9}$$

Substituting Eq. 2.5 and 2.6 into Eq. 2.9 we get

$$\mathbf{W_{av}} = \mathbf{\hat{a}_r}\eta\frac{|I_0|^2}{8\pi^2 r^2}\left[\frac{\cos\left(\frac{kl}{2}\cos\theta\right) - \cos\left(\frac{kl}{2}\right)}{\sin\theta}\right]^2 \tag{2.10}$$

Substituting Eq. 2.10 into Eq. 2.8 the far field radiation intensity of the finite length dipole is

$$U(\theta,\phi) = \eta\frac{|I_0|^2}{8\pi^2}\left[\frac{\cos\left(\frac{kl}{2}\cos\theta\right) - \cos\left(\frac{kl}{2}\right)}{\sin\theta}\right]^2 \tag{2.11}$$

The total radiated power is the average power density vector integrated over a sphere. Integrating Eq. 2.11 over a sphere we get

$$P_{rad} = \eta\frac{|I_0|^2}{4\pi}\int_0^{\pi}\frac{\left[\cos\left(\frac{kl}{2}\cos\theta\right) - \cos\left(\frac{kl}{2}\right)\right]^2}{\sin\theta}d\theta \tag{2.12}$$

which expands to

$$\begin{aligned} P_{rad} = \eta\frac{|I_0|^2}{4\pi}&\left[\gamma + \ln(kl) - \mathrm{Ci}(kl) + \frac{1}{2}\sin(kl)\mathrm{Si}(kl)\right]\ldots \\ &+ \frac{1}{2}\cos(kl)\left[\gamma + \ln\left(\frac{kl}{2}\right) + \mathrm{Ci}(2kl) - 2\mathrm{Ci}(kl)\right] \end{aligned} \tag{2.13}$$

where $\mathrm{Ci}(x)$ is the cosine integral $\mathrm{Ci}(x) = -\int_x^{\infty}\frac{\cos y}{y}dy$ and $\mathrm{Si}(x)$ is the sine integral $\mathrm{Si}(x) = \int_0^x \frac{\sin(y)}{y}dy$.

The closed-form expression for the gain of an ideal half-wavelength dipole is found by substituting eq. 2.11 and 2.13 into eq. 2.7 and setting $l = \pi/2$ and $e_{cd} = 1$:

$$G(\theta,\phi) = \frac{4}{\mathrm{Cin}(2\pi)}\left[\frac{\cos\left(\frac{\pi}{2}\cos\theta\right)}{\sin\theta}\right]^2 \tag{2.14}$$

where $\mathrm{Cin}(x)$ is the cosine integral $\mathrm{Cin}(x) = \int_0^x \frac{1-\cos(y)}{y}dy$. Figure 2.2 shows the far-field gain vs. θ of a half-wavelength dipole. The maximum gain is at $\theta = [-90, 90]$ and the gain does not vary as a function of ϕ.

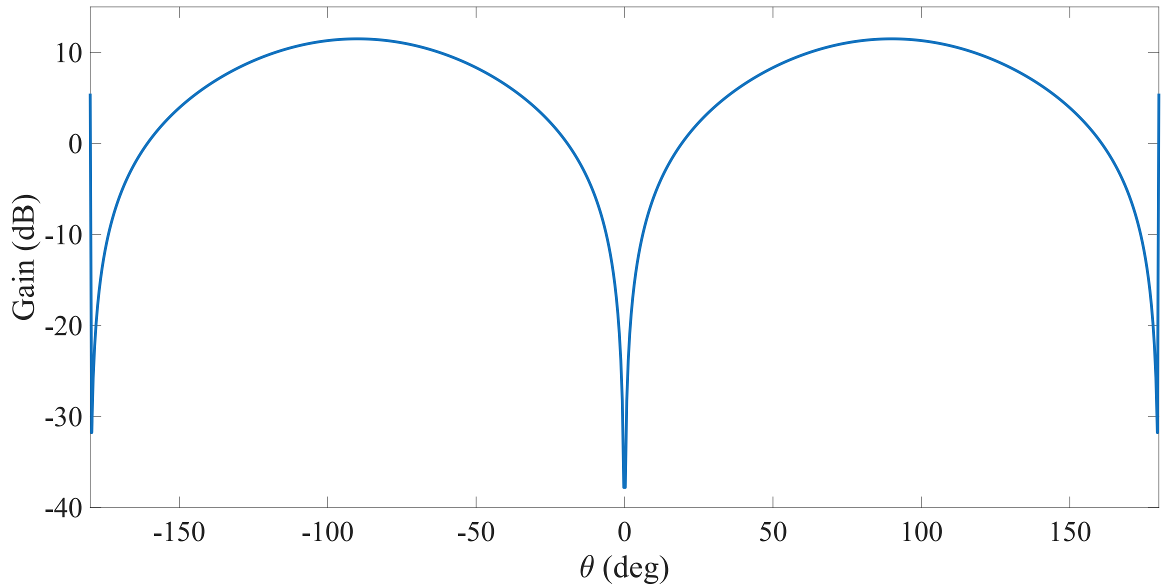

Figure 2.2: Far-field gain of a half-wavelength dipole antenna located at the origin with wires running parallel to the z-axis vs. the polar angle

2.3.2 Patch

The simulation also supports a patch antenna model simulated in Ansys HFSS to obtain near-field radiation fields or the far-field gain. The HFSS model is shown in Fig. 2.3. The gain is then exported to a comma-separated values file and imported into Python as a lookup table based on the relative angle of regard between the element and the scatterer. The far-field gain calculation from HFSS is used for patch simulations in this paper because the nearest target (1 meter) is distant enough to disregard the reactive component of the antenna response.

To validate the use of the far-field gain values, we exported the NearPoyntingTotal values for spheres at 3-1200 cm, calculated gain values using the NearPoyntingTotal values, and compared them to the far-field gain values. The results of those comparisons are shown in Fig. 2.4. To calculate the gain values from the NearPoyntingTotal values, we used the relation from Balanis [15]

$$G = 4\pi \frac{U(\theta, \phi)}{P_{acc}} \tag{2.15}$$

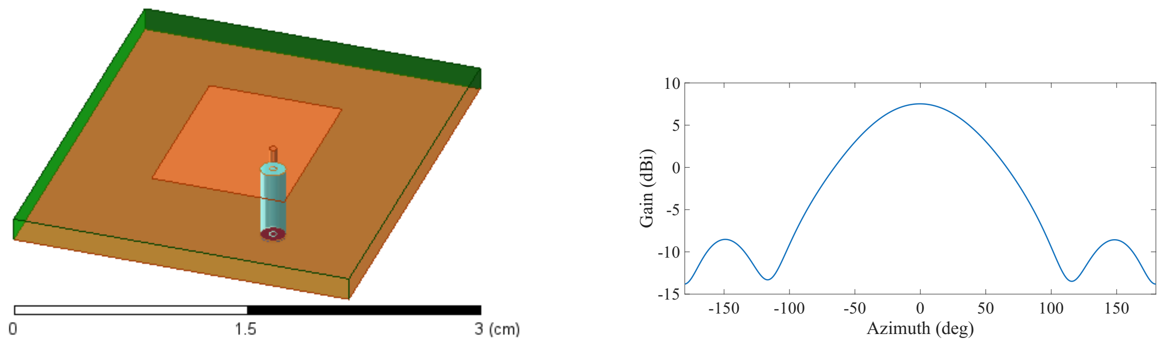

(a). Patch Antenna (b). Antenna Pattern

Figure 2.3: 10 GHz patch antenna modeled in HFSS

where P_{acc} is the accepted power and $U(\theta, \phi)$ is the directivity given by

$$U(\theta, \phi) = r^2 W_{av}. \tag{2.16}$$

W_{av} is the average radiated power, which is calculated by HFSS as NearPoynting-Total. Fig. 2.4 shows the difference between the near-field calculated gain and the far-field gain vs. range.

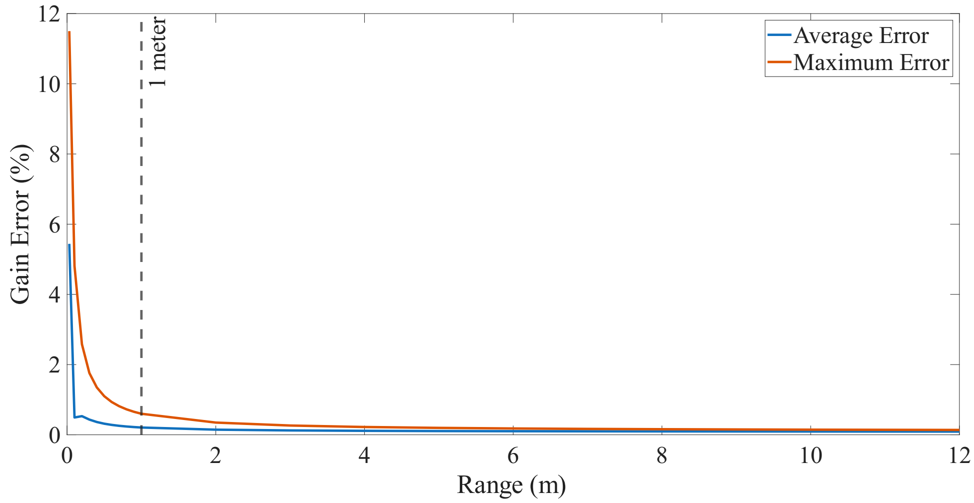

Figure 2.4: Error between the gain calculated from near-field values and the far-field gain

Chapter 3

Beamforming Algorithms

3.1 Far Field Beamforming

Beamforming for MIMO arrays is achieved during post-processing by taking the Fourier transform of the complex-valued fast-time array after pulse compression and applying a phase correction to each transmit-receive pair. Fig. 3.1 shows how the phase correcting weights for each element are calculated using the far field assumption of a plane wave reflecting back from the target. The plane wave estimation is valid because the array size compared to the diameter of the spherical wavefront is so small that the phase difference at each element between the actual spherical wavefront and a theoretical plane wave is negligible. Since the target is somewhere to the left of the array in this figure, the distance from the target to each element in the array becomes longer as we traverse the array from left to right. In an equally spaced phased array, the phase weights can be expressed as

$$\psi_n(\theta) = e^{-j2\pi nd\cos\theta/\lambda} \tag{3.1}$$

where n is the element in the phased array numbered from left to right and θ is the direction the beam is steered toward. For an array of arbitrary spacing, the $nd\cos\theta$ term can be replaced by the dot product of the unit vector for the beam steering angle and the Cartesian coordinates of the n_{th} array element.

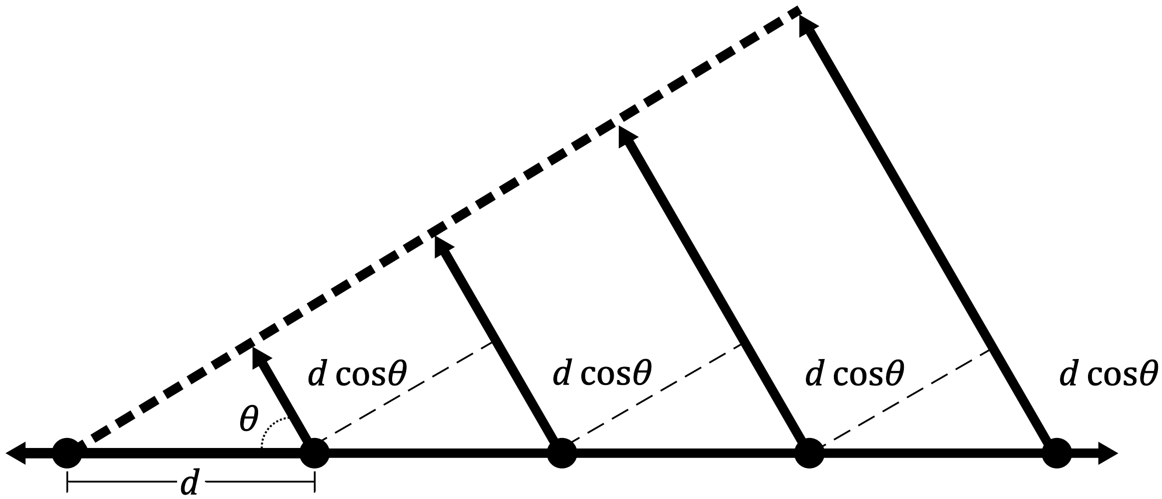

Figure 3.1: Far-field Beamforming

3.2 Nearfield Beamforming

To focus a target response with minimal near-field sidelobes, a beamforming algorithm that accounts for the spherical nature of the scattered wavefront is required. As with conventional far-field beamforming, the returns from each array element must be phase-aligned to compensate for the spatial separation of the elements and the desired beam angle. However, when the far-field plane-wave assumption is no longer valid, the focusing operation becomes explicitly range dependent. Figure 3.2 illustrates the geometry of a point scatterer producing a spherical wavefront incident on a uniform linear array. Grosicki [16] gives the relative propagation delay for element n with respect to the array phase center as

$$\tau_n = \frac{r}{v_p}\left(\sqrt{1+\frac{d_n^2}{r^2}-\frac{2d_n\sin\varphi}{r}}-1\right) \tag{3.2}$$

where τ_n is the differential propagation delay between the nth element and the array phase center, d_n is the position of the nth element along the array, r is the target range, v_p is the propagation velocity, and φ is the look angle of the target. Since (3.2) is explicitly range dependent, digital near-field beamforming using this formulation must be performed independently for each range bin. For a MIMO array, the differential delays must be computed separately for each transmitting element (radiator) and each receiving element (collector) for a given look angle and range. After applying a discrete Fourier transform along the fast-time dimension, the received data for a given transmitter–receiver pair can be phase-compensated in the frequency domain by

$$\psi_{rad,col}(f_r) = e^{j\,2\pi(f_r+f_0)\left(\tau_{\text{rad}}+\tau_{\text{col}}\right)} \tag{3.3}$$

where f_r denotes the range-frequency, f_0 is the RF carrier (or equivalent center frequency of the transmitted waveform), τ_{rad} is the relative delay associated with the transmitting element, and τ_{col} is the relative delay associated with the receiving element. The f_r term in the exponential aligns the peaks formed by the matched filter for each virtual array channel, while the f_0 term adjusts the phase. The far-field beamforming algorithm only includes the phase adjustment and does not align the peaks of the matched filter outputs. After applying this phase compensation, an inverse Fourier transform is performed to return the data to the fast-time/slow-time domain, and the range bin corresponding to the focusing range r is extracted. This process must be repeated for all desired look angles, all transmit–receive element pairs, and all range bins to form a near-field-focused range–azimuth image.

For computational efficiency, a transition range can be defined beyond which conventional far-field beamforming is applied, since the spherical wavefront model converges to the plane-wave approximation at sufficiently large ranges. The transition point would be defined in terms of the radar aperture size. A nominal point would be a range approximately 10 times the largest dimension of the MIMO array, which could be adjusted according to the system's sidelobe and beamwidth requirements. Similarly, range bins can be processed in groups using the same range value to gain computational efficiency at the expense of higher sidelobes and a wider beam width.

The spherical beamforming algorithm is summarized by looping through the following steps for each range bin:

- Determine range associated with range bin to be processed
- Calculate total distance of travel for each transmit/receive channel from transmitter to point in space based on desired beam angle and range
- Apply phase and range delay to each channel based on the distance of travel
- Perform inverse Fourier transform on the fast time dimension of the phase-adjusted array
- Store the processed range bin in the image array

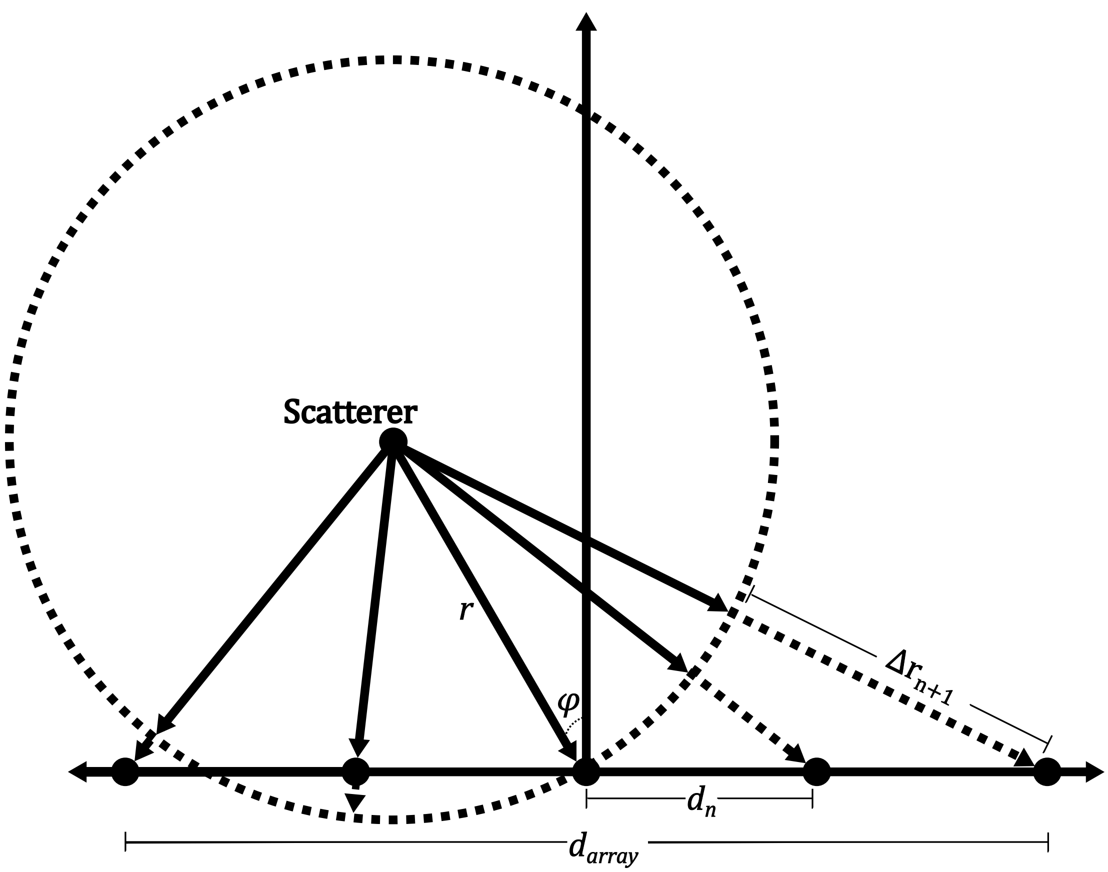

Figure 3.2: Near-field Beamforming

Chapter 4

Description of MIMO Radar System Simulation

4.1 Code Structure

The primary work for this thesis is a MIMO radar system simulation environment developed in Python. Fig. 4.1 shows a block diagram of the code structure. This chapter will describe how the MIMO lattice and transmit waveform, and target environment are defined, and how the signals are simulated as they propagate from the transmitter to the target environment and finally to the receiver for digital beamforming.

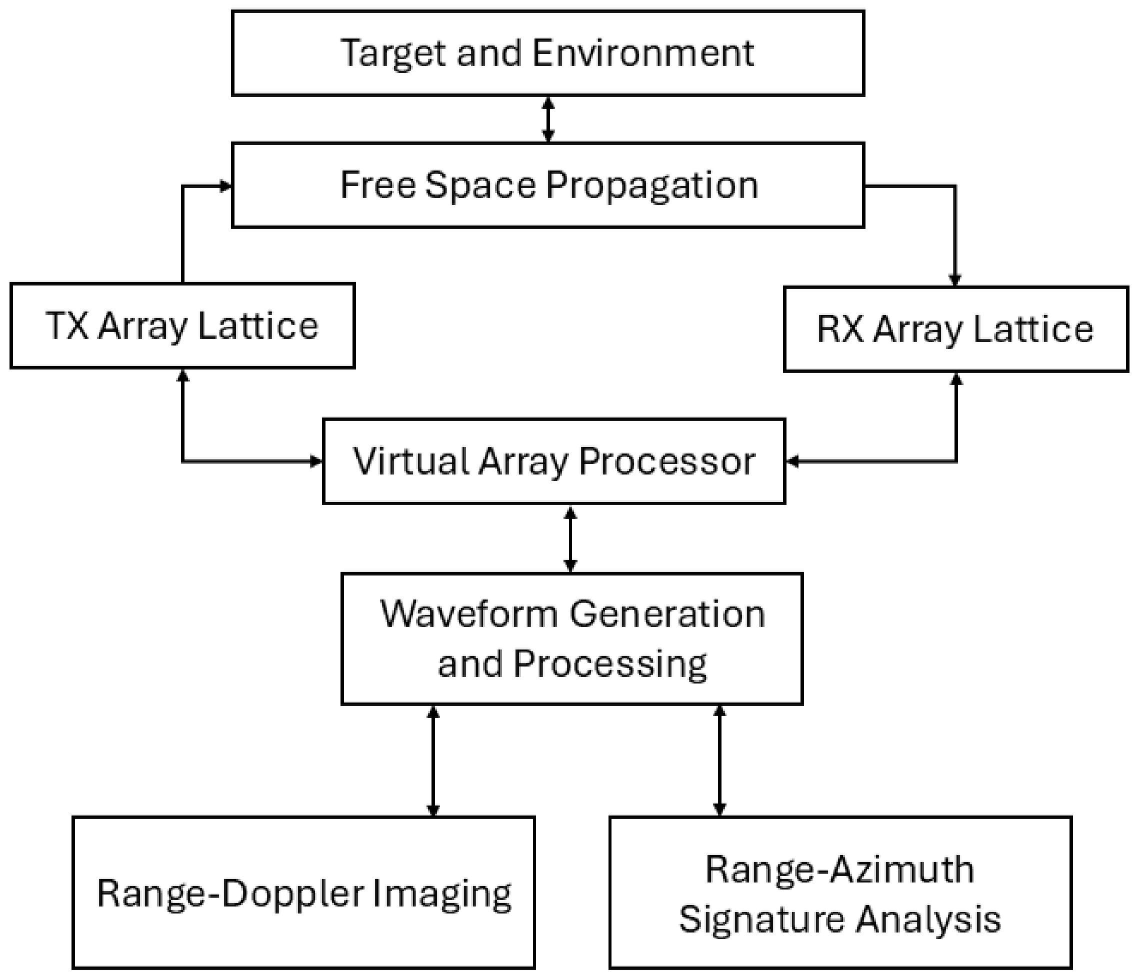

Figure 4.1: Simulation Code Structure

4.2 Waveform Generation

MIMO lattices form virtual arrays by transmitting orthogonal waveforms from each transmit subarray and including a bank of matched filters for each transmit waveform on the load attached to each receive element. Achieving waveform orthogonality for MIMO applications has been extensively studied [17] [18] [19]. This work will assume that each transmitter modulated the waveform with perfect orthogonality and that the matched filters separate the waveforms without loss. The transmit waveform used in this study is a 10 GHz linear frequency-modulated (LFM) pulse occupying 1 GHz of bandwidth. The LFM pulse waveform can be expressed mathematically as

$$\tilde{a}(t) = w(t) \cos \left(2\pi \left(f_0 - \frac{\beta}{2} \right) t + \pi \frac{\beta}{T_p} t^2 \right) \tag{4.1}$$

where $w(t)$ is the window function of the pulse, f_0 is the center frequency of the LFM signal, β is the bandwidth of the LFM signal and T_p is the pulse width. The LFM pulse waveform has a complex envelope of

$$a(t) = w(t) e^{\left(-2\pi j \left(\frac{\beta}{2} \right) t + j\pi \frac{\beta}{T_p} t^2 \right)}. \tag{4.2}$$

The simulator generates a complex array representing the output of the in-phase and quadrature analog-to-digital converters attached to the transmitter. The user defines the center frequency (f_0), pulse width (T_p), bandwidth (β), and analog-to-digital sampling rate (F_{adc}). To generate the transmit pulse array, the simulator first creates a smoothed amplitude pulse envelope as the convolution of a rectangular pulse ($L_{pulse} = T_p / T_{adc}$) with a Hanning window that is 5% of the length of the rectangular pulse (L_w). The pulse envelope is then normalized according to

$$\mathbf{P_{env}} = \frac{\mathbf{L_w} \bigotimes \mathbf{L_{pulse}}}{||\mathbf{L_w} \bigotimes \mathbf{L_{pulse}}||_\infty}. \tag{4.3}$$

The pulse time array, T_{pulse}, is created by dividing an array of consecutive integers starting at 0 that is the length of the pulse envelope (L_{env}) by F_{adc}. Then the chirp function is calculated using the expression

$$\mathbf{v_{chirp}} = e^{-2\pi j \frac{\beta \mathbf{L_{pulse}}}{2 T_p F_{adc}} \mathbf{T_{pulse}}} e^{\pi j \beta \frac{\mathbf{T_{pulse}}^2}{T_p}}. \tag{4.4}$$

The final LFM transmit array is the product of v_{chirp} and P_{env}.

4.3 Waveform Propagation Environment

4.3.1 MIMO Lattice

The MIMO lattice is user-defined. The user defines the number of elements in each subarray, the spacing of the elements within the subarray, and the spacing of the subarrays. Finally, the user defines the locations of the subarray along the x, y, or z axis as a binary array where ones denote a position where a subarray is located, and zeros denote a position where a subarray is not located. The MIMO function then generates arrays of tuples for the locations of each transmit subarray and each receive subarray. A matrix is also generated for the positions of the virtual array elements by convolving the transmit and receive positions and assigning transmit and receive indices to each virtual array element corresponding to the transmit and receive subarrays that created it. Duplicate virtual array elements are discarded to simplify beamforming.

4.3.2 Mutual Coupling

The simulation environment also considers mutual coupling of the transmit and receive arrays. Mutual coupling is a phenomenon where radiation from one antenna induces currents in nearby antennas, weakly re-radiating the transmitted signal from each of those antennas and creating voltages on any loads attached to them.

Mutual coupling between dipole antennas was modeled using the methodology developed by Arnold [20]. Because this thesis is not concerned with mitigating mutual coupling with matching circuits, the system model used by Arnold is simplified by setting the source and load reflection coefficients to zero and assuming the S-parameters of the transmit matching circuit, receive matching circuit, and the receiver low noise amplifier are

$$\mathbf{S} = \begin{bmatrix} 0 & 1 \\ 1 & 0 \end{bmatrix}. \tag{4.5}$$

Under these assumptions, the linear operator that transforms voltages on the source to currents in the transmit antennas becomes

$$\mathbf{D}^{(\mathbf{T})} = \frac{1}{Z_0}[\mathbf{I} - \mathbf{S}_{\mathbf{A}}^{(\mathbf{T})}] \tag{4.6}$$

where $Z_0 = 50\Omega$ is the characteristic impedance of the system, $\mathbf{I}$ is the identity matrix, and $\mathbf{S}_{\mathbf{A}}^{(\mathbf{T})}$ is the S-parameter matrix of the transmit antenna array. The linear operator that transforms open-circuit voltages on the receive antennas to voltages on the loads also becomes

$$\mathbf{D}^{(\mathbf{R})} = \frac{1}{2}[\mathbf{I} - \mathbf{S}_{\mathbf{A}}^{(\mathbf{R})}] \tag{4.7}$$

where $\mathbf{S}_{\mathbf{A}}^{(\mathbf{R})}$ is the S-parameter matrix of the receive antennas.

The S-parameters of the transmit and receive arrays are generated by finding the Z-parameters using the closed-form expressions for self impedance as $Z_{11} = 73+j42.5$ and mutual impedance (Z_{12}) of half-wavelength dipole antennas [15] as

$$\begin{aligned} Z_{12} &= \tfrac{\eta}{4\pi}[2\mathrm{Ci}(u_0) - \mathrm{Ci}(u_1) - \mathrm{Ci}(u_2)] - \tfrac{j\eta}{4\pi}[2\mathrm{Si}(u_0) - \mathrm{Si}(u_1) - \mathrm{Si}(u_2)] \\ u_0 &= kd \\ u_1 &= k(\sqrt{d^2 + (\pi/2)^2} + \pi/2) \\ u_2 &= k(\sqrt{d^2 + (\pi/2)^2} - \pi/2) \end{aligned} \tag{4.8}$$

where d is the distance between the antennas. The Z-parameters are then converted to S-parameters by solving the equation

$$\left\{[\mathbf{Z}]\left[\frac{\mathbf{I}}{\sqrt{Z_0}}\right] + [\mathbf{I}][\sqrt{Z_0}]\right\}\{\mathbf{S}\} = [\mathbf{Z}]\left[\frac{\mathbf{I}}{\sqrt{Z_0}}\right] - [\mathbf{I}][\sqrt{Z_0}] \tag{4.9}$$

for $\mathbf{S}$.

4.3.3 Target Definition

The free-space propagation environment is modeled as a vacuum in this simulation for simplicity. All scatterers are user-defined point objects with a starting position in 3-d space, a constant velocity vector, and a radar cross section. Scatterers are not modeled to cast shadows, so if they are lined up at varying ranges along the same look angle from the array, they will each be simulated to reflect energy back to the array as though the others were not present. Target positions are updated in the simulation for each pulse.

For each target and transmitter/receiver pair and pulse, a reflection coefficient is calculated according to the radar range equation to determine the magnitude of the signal as it arrives at the receiver load:

$$\alpha_{Tx,Rx,Target,Pulse} = \sqrt{\frac{G_{Tx,\theta_{Tx},\phi_{Tx}} G_{Rx,\theta_{Rx},\phi_{Rx}} \lambda^2 \sigma_{Target}}{(4\pi)^3 r_{Target}^4}} \tag{4.10}$$

where $G_{Tx,\theta_{Tx},\phi_{Tx}}$ is the gain of the transmit antenna in the direction of the target, $G_{Rx,\theta_{Rx},\phi_{Rx}}$ is the gain of the receive antenna in the direction of the target, σ_{Target} is the target radar cross section and r_{Target} is the range from the array phase center to the target. The signal delay for each target, transmitter/receiver pair, and pulse is also calculated by summing the range from the transmitter to the target with the range from the receiver to the target and dividing that sum by the velocity of propagation:

$$\tau_{Tx,Rx,Target,Pulse} = (r_{Tx,Target,Pulse} + r_{Rx,Target,Pulse})/c. \tag{4.11}$$

To account for the signal delay, τ, we must take the Fourier transform of the transmitted signal and delay its position in the receiver signal array and its phase, then take the inverse Fourier transform to achieve the fast-time array:

$$H_{Tx,Rx,Target,Pulse} = \mathcal{F}^{-1}\left\{\mathcal{F}\{\mathbf{a_{Tx}}\} e^{-2\pi j \tau_{Tx,Rx,Target,Pulse}(\mathbf{f_{axis}}+f_0)}\right\} \tag{4.12}$$

where $\mathcal{F}(\cdot)$ denotes the Fourier transform, f_0 is the center frequency, and $\mathbf{f_{axis}}$ is the range-frequency axis given by

$$\mathbf{f_{axis}} = -\frac{1}{2}F_{adc} + [0 : N_{adc}]\frac{F_{adc}}{N_{adc}}. \tag{4.13}$$

The voltage at receiver load Rx for each transmitter Tx for each pulse is then calculated using

$$v_{Tx,Rx,Pulse} = \sum_{q}^{N_q} \alpha_{Tx,Rx,q,Pulse} H_{Tx,Rx,q,Pulse} \tag{4.14}$$

if mutual coupling is not considered. Where N_q is the number of targets, $\mathbf{a_{Tx}}$ is the signal transmitted by transmitter Tx, $\mathcal{F}\{\cdot\}$ signifies the Fourier transform, and $\mathcal{F}^{-1}\cdot$ signifies the inverse Fourier transform. The voltage at the receiver load Rx for each transmitter Tx for each pulse, taking mutual coupling into account, is

$$\mathbf{v_{Tx,Rx,Pulse}} = \sum_{l}^{N_R}\sum_{q}^{N_q}\sum_{m}^{N_T} D^{(R)}_{Rx,l} D^{(T)}_{Tx,m} \alpha_{m,l,q,Pulse} H_{m,l,q,Pulse}. \tag{4.15}$$

In a real MIMO system transmitting orthogonal waveforms, the final receiver load for each Rx channel would be a sum of every transmitter pulse:

$$\mathbf{v_{Rx,Pulse}} = \sum_{m}^{N_T} \mathbf{v_{m,Rx,Pulse}}. \tag{4.16}$$

The transmit channels on each receiver would be separated by matched filters, taking advantage of the transmitter orthogonality. The subject of waveform orthogonality is an active and fruitful field of research [21–23]. This work will assume the ideal, and as of yet impossible, scenario that the transmit waveforms are perfectly separated by the matched filter in the receiver and so the simulator treats every transmit waveform as a simple LFM and keeps them separate by never performing the summation in eq. 4.16.

4.4 Receiver

The receiver has a user-defined gain and noise figure. The function receiver calculates the noise power from the noise figure using the relation from [24]

$$P_n = F_n k T_0 B G_a. \tag{4.17}$$

Where F_n is the linear noise figure, T_0 is the reference temperature 290° Kelvin, B is the receiver bandwidth assumed to be half the sampling rate of the analog-to-digital converter, and G_a is the linear receiver gain. This simulation does not consider other noise sources such as phase noise from scatterers, thermal noise from the antenna, waveguides, filters, or transmitter.

To generate the noise, the simulation generates two arrays of random numbers from 0-1 on the standard normal distribution. The arrays are the same size as the unprocessed fast-time/slow-time array generated in the waveform propagation environment. One of the arrays is real, and the other array is imaginary. The receiver noise output is then calculated as

$$\mathbf{N_{out}} = \sqrt{P_n/2}(\mathbf{a_{nr}} + j\mathbf{a_{ni}}) \tag{4.18}$$

where $\mathbf{a_{nr}}$ is a standard normal distribution of random real numbers from 0 to 1 and $j\mathbf{a_{ni}}$ is a standard normal distribution of random imaginary numbers from $j0$ to $j1$. The receiver output is the input signal multiplied by the linear receiver gain and summed with the receiver noise as given by

$$\mathbf{a_r^{Tx,Rx,Pulse}} = \mathbf{v_{Tx,Rx,Pulse}} G_a + \mathbf{N_{out}}. \tag{4.19}$$

4.5 Matched Filter

In a MIMO system, matched filters are used to separate the contribution of the transmit signals on each receiver load into transmit/receive pairs. The matched filters simultaneously provide pulse compression, creating the bandwidth-dependent range resolution. In a digital receiver, as is simulated in this work, the matched filter is set up by sampling each transmit signal, reversing the sequence of the samples, and taking the complex conjugate of each sample. The matched filter is then convolved with the sampled receive signal so that peaks form at the range bins corresponding to the source of target echoes.

4.6 Beamforming

Both the far-field beamforming, relying on the plane wave estimation, and the near-field beamforming methods described in Chapter 3 are implemented in the simulation environment. The user may define a max range beyond which the simulation transitions from the near-field method to the far-field method. The user may also define a range interval over which the simulation will apply the near-field method, with a minimum of one range bin. The custom range interval and maximum range features of the near-field beamforming method are purely for computational expediency. Increasing the range interval widens the gap between the range used in the algorithm and the actual range of target echoes, thereby broadening the main beam and increasing sidelobe levels. Setting a maximum range will create a discontinuity in which the sidelobe levels and the half-power beamwidth of the main beam increase as the algorithm transitions from the near-field to the far-field method. Both methods are implemented after matched filtering. The user defines a range of look angles to process, and the simulation iterates over them. The specified beamforming method is applied to the matched-filtered fast-time slow arrays of each transmit/receive pair for each iteration of the look angle loop.

Far-field beamforming first calculates the phase weights of each element of the virtual MIMO array using Eq. 3.1. A fast-time Fourier transform is applied to the matched-filtered fast-time/slow-time arrays for each transmit/receive pair and then multiplied by the corresponding phase weight. An inverse Fourier transform is applied to the final result and the fast-time/slow-time arrays associated with each transmit/receive pair are summed to create a fast-time/slow-time array associated with that look angle. The algorithm is mathematically represented as

$$\mathbf{a}_{\mathbf{beam}}^{\theta,\phi,\mathbf{Pulse}} = \sum_{m}^{N_a} \mathcal{F}^{-1}\{\mathcal{F}[\mathbf{a}_{\mathbf{r}}^{\mathbf{m},\mathbf{Pulse}}]\psi(m)\}. \tag{4.20}$$

The Fourier transform and inverse Fourier transform are not strictly necessary for the far-field algorithm since it operates on the match-filtered response and does not include a range-alignment of the peaks of the match filter outputs. This implementation was chosen to mirror the spherical beamforming process, which does include the range alignment, and therefore does require a frequency domain operation.

The near-field beamforming algorithm loops through each focusing range, defined by the minimum range, maximum range, and the focusing range interval. At each focusing range, the algorithm calculates the propagation delay from each transmitting and receiving antenna according to the look angle using Eq. 3.2 and uses that to calculate the weights according to Eq. 3.3. The near-field beamforming algorithm computes a fast-time Fourier transform of the matched-filter output for each transmit/receive pair and applies the phase weights to it at each iteration of the focusing range loop. The program then takes the inverse Fourier transform of the result and populates the range bins corresponding to the final fast-time/slow-time array's focusing range for each transmit/receive pair. Once the user-specified maximum focusing range has been processed, the far-field beamforming algorithm is used to populate any remaining range bins. Finally, the fast-time/slow-time arrays for each transmit/receive pair are summed to produce the fast-time/slow-time array for the look angle. A range-azimuth map is created by summing the fast-time arrays for each pulse per look angle so that the 3-dimensional fast-time/slow-time/angle array collapses to a fast-time/angle array.

4.7 Range-Doppler Processing

The output of the beamforming algorithm as a fast-time/slow-time/angle array can be processed into a range-Doppler map, particularly if the user-defined targets were given a non-zero velocity. The first step is to sum the fast-time/slow-time arrays element-wise across all the look angles to create a single composite fast-time/slow-time array. Then apply a slow-time Fourier transform to the composite fast-time/slow-time array to produce a fast-time/Doppler array. The Doppler axis can be interpreted as velocity by multiplying an array of consecutive integers centered on zero sized to the number of pulses by the relation

$$\mathbf{v_{axis}} = \frac{N_{axis} v_p}{2 N_p T_r} \tag{4.21}$$

where N_{axis} is an array of consecutive integers centered on zero and sized to the number pulses, v_p is the velocity of propagation, N_p is the number of pulses, and T_r is the pulse repetition interval. The fast-time/Doppler array processing can be expressed mathematically as

$$\mathbf{a}_{\mathbf{beam}}^{\mathbf{dopp}} = \mathcal{F}_{st} \left\{ \sum_{m}^{N_{\theta,\phi}} \mathbf{a}_{\mathbf{beam}}^{\theta,\phi} \right\}. \tag{4.22}$$

Here, $\mathcal{F}_{st}$ is the slow-time Fourier transform and $N_{\theta,\phi}$ is the number of look angles processed for beamforming.

4.8 Target Detection

The peak sidelobe level of the array factor of the MIMO lattice studied in this work is approximately -12 dB. This presents a detection challenge: setting the detection threshold high enough to prevent sidelobe energy from triggering a detection risks losing smaller targets. Setting the threshold low enough to detect low-RCS targets would cause high-RCS targets to appear in multiple directions on the detection map due to sidelobe energy. The 12 dB of dynamic range between the peak sidelobes and the main beam also creates the need for sensitivity time control (STC) to normalize returns with respect to range so that targets of similar RCS can be detected at 1 meter and at 60 meters, which would otherwise require a dynamic range of 71 dB.

Since this is a pulsed Doppler radar with coherent pulse integration and pulse compression, dynamically adjusting the receiver gain does not effectively mitigate this issue. Therefore, this simulation implements a virtual STC by multiplying the final range-azimuth or range-Doppler array by the square of the range-axis element-wise. This flattens the dynamic range of returns with respect to distance to the target. The output of that range normalization is then further normalized to the maximum return, converted to decibels, and then checked against a threshold of -11 dB. This allows the largest RCS scatterer to appear on the display without sidelobe clutter, and includes any other scatterers with at least 28% of the largest scatterer's RCS.

An adaptive detection approach based on a constant false alarm rate (CFAR) would be preferred to overcome fluctuations in the noise and the propagation environment. However, CFAR methods will pick up sidelobes as false detections unless they fall below the noise floor. If the noise floor was set such that the angular sidelobes were below the noise floor, the dynamic range for targets of similar RCS would be less than 1 meter. This work explores a 60-meter detection window. A simple CFAR implementation would require detecting all sidelobe clutter from close (or high RCS) targets to detect far (or low RCS) targets. [25, 26] Implementation of adaptive target detection and sidelobe reduction is left for future work.

Chapter 5

Results and Data Analysis

5.1 Range-Azimuth Processing

All simulations in this work will utilize the MIMO lattice shown in Fig. 2.1. All the simulations will also use the same LFM waveform occupying 9.5 - 10.5 GHz, corresponding to a fractional bandwidth of 10%. Scatterer locations are given in spherical coordinates with the phase center of the MIMO virtual antenna array located at the origin as shown in Fig. 5.1 where r' is the distance from the phase center of the array to the scatterer, θ' is the angle between the line formed by the origin and the target location and the z-axis, and ϕ' is the angle of rotation of the radial line around the z-axis. The half-wavelength dipoles of the MIMO array are arranged along the y-axis with the dipoles perpendicular to the z-axis. All targets are located on the $\theta' = 90^\circ$ plane.

To demonstrate the operation of the range-azimuth, we set up a propagation environment with 15 stationary scatterers, each with an RCS of 10 m^2 spaced 4 meters apart, starting at the $r' = 1$ meter range and aligned with the $\phi' = 0^\circ$ azimuth look angle. The amplifier was defined with a 1.5 dB noise figure and a gain of 33 dB, based on the specification of MACOM MAAL-011272. Fig. 5.2 demonstrates the processing stages of the threshold detection process. The range-azimuth maps were generated using the planar beamforming algorithm described in Ch. 3.

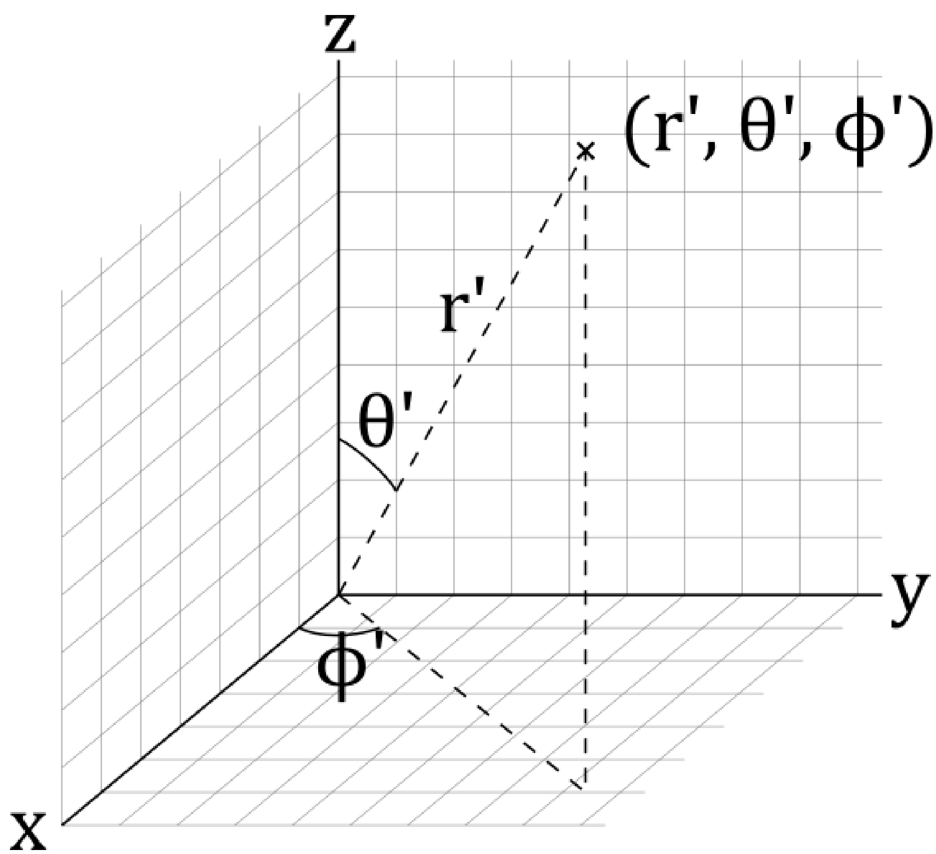

Figure 5.1: Spherical coordinate system used to define scatterer locations. r' is the radial distance from the phase center of the virtual array to the scatterer and the z-axis is the polar axis. All array elements are arranged along the y-axis and half-wavelength dipoles are aligned with the z-axis.

Fig. 5.2(a) shows the raw beamforming output, normalized to the maximum return. The signature of the nearest scatterer, located at a range of 1 meter, is almost completely unfocused, highlighting the limitations of planar beamforming for detecting close-range objects. There is a dynamic range of over 70 dB between the nearest scatterer (1 meter) and the farthest scatterer (57 meters). The peak azimuth sidelobes are approximately -12 dB.

Fig. 5.2(b) normalizes the output shown in Fig. 5.2(a) by range by multiplying each azimuth column vector by the square of the range axis. This range normalization equalizes the magnitude of the returns across the range. Since all the targets have the same RCS, they show up with the same absolute signal strength; the signal-to-noise ratio still decreases at the same rate with respect to range because the noise is included in the range normalization.

Fig. 5.2(c) shows the output of the threshold detection after each range-azimuth bin in Fig. 5.2(b) is compared to a threshold of -11 dB. The nearest scatterer shows up at the 12° azimuth look angle due to the breakdown of the plane wave estimation at that range. The peak sidelobes corresponding to the scatterer located at 5 meters are detected by the threshold detection logic in addition to the main beam. The remaining targets are correctly located by the threshold-based detection logic.

Fig. 5.3 was generated uses the same simulation parameters as Fig. 5.2 but without mutual coupling to demonstrate how the implementation of mutual coupling in the half-wavelength dipole model affects the simulation output.

Fig. 5.4 was generated using the same waveform parameters and propagation environment used for Fig. 5.2, but with a patch antenna instead of a half-wavelength dipole to demonstrate the simulation capability. The half-wavelength dipole is used for the rest of this paper because mutual coupling was implemented for that model. Simulating a full MIMO array in a computational electromagnetics program would be necessary to implement mutual coupling for an array of patches.

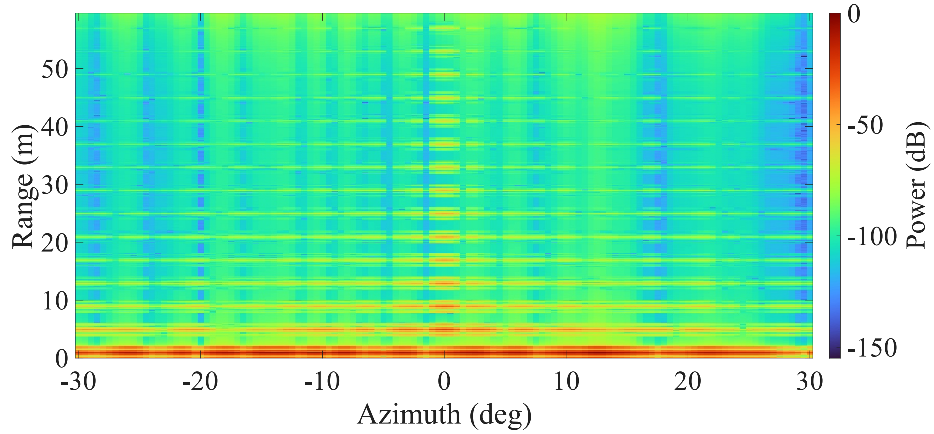

(a). Range-azimuth map normalized to the maximum return

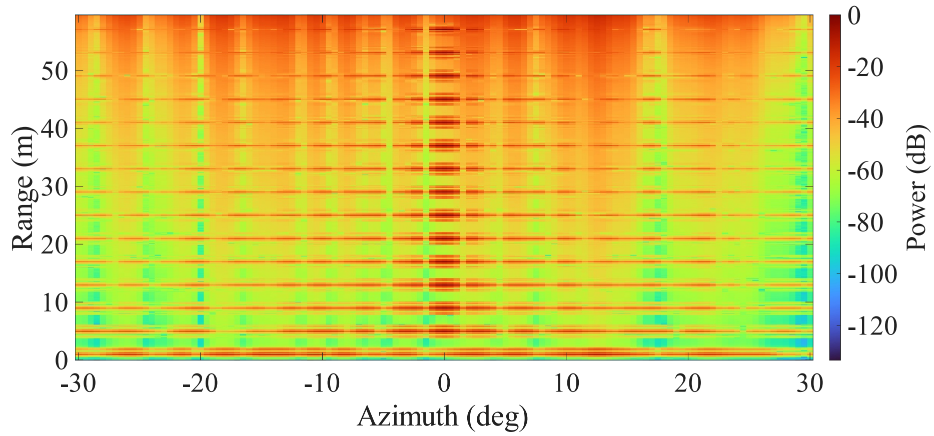

(b). Range-azimuth map with range-adjusted signal

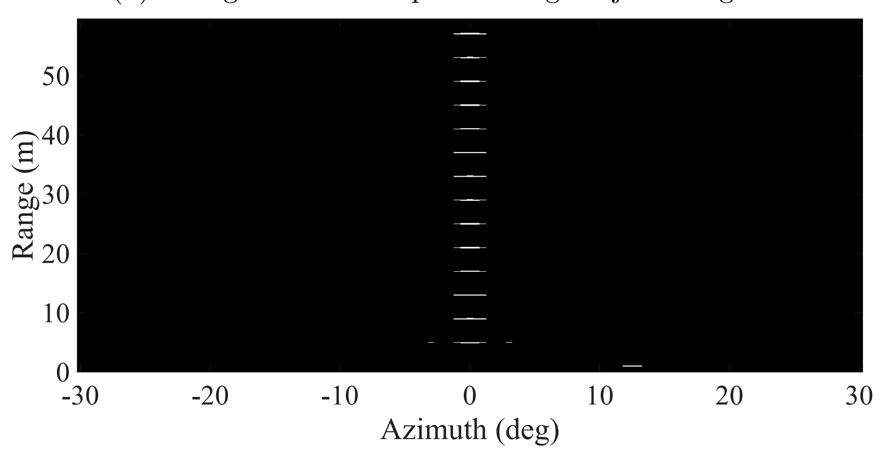

(c). Range-azimuth map with threshold detection

Figure 5.2: Range-azimuth maps showing the stages of threshold detection using 15 scatterers spaced 4 meters apart along $\phi' = 0^\circ$ and $\theta' = 90^\circ$ processed with planar beamforming on a MIMO dipole lattice

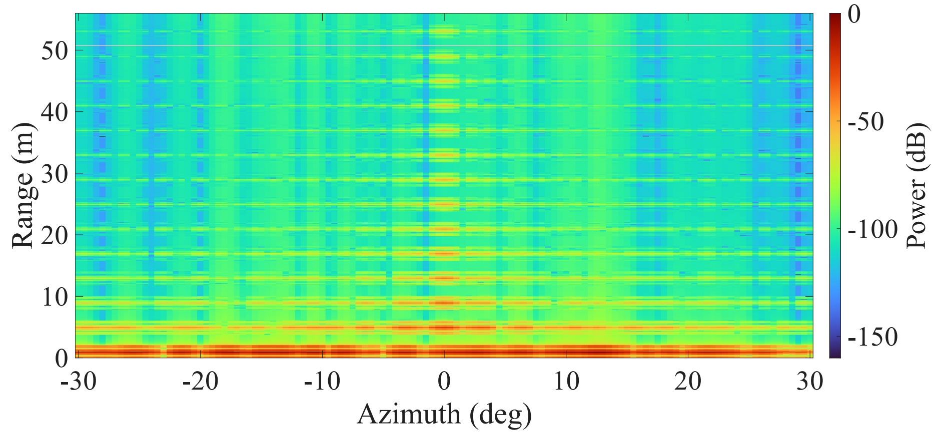

(a). Range-azimuth map normalized to the maximum return

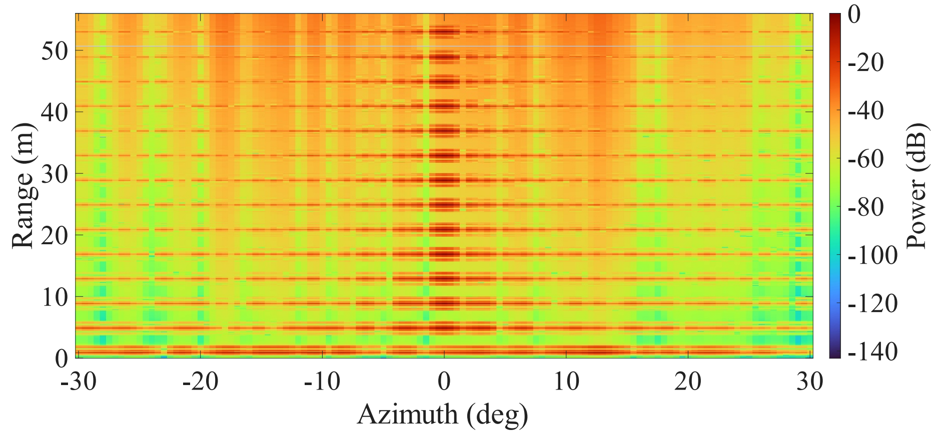

(b). Range-azimuth map with range-adjusted signal

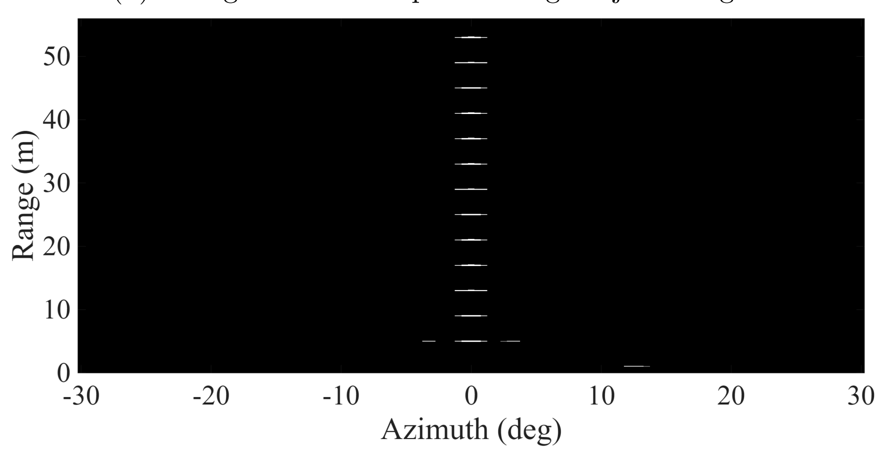

(c). Range-azimuth map with threshold detection

Figure 5.3: Range-azimuth maps showing the stages of threshold detection using 15 scatterers spaced 4 meters apart along $\phi' = 0^\circ$ and $\theta' = 90^\circ$ processed with planar beamforming on a MIMO dipole lattice without mutual coupling

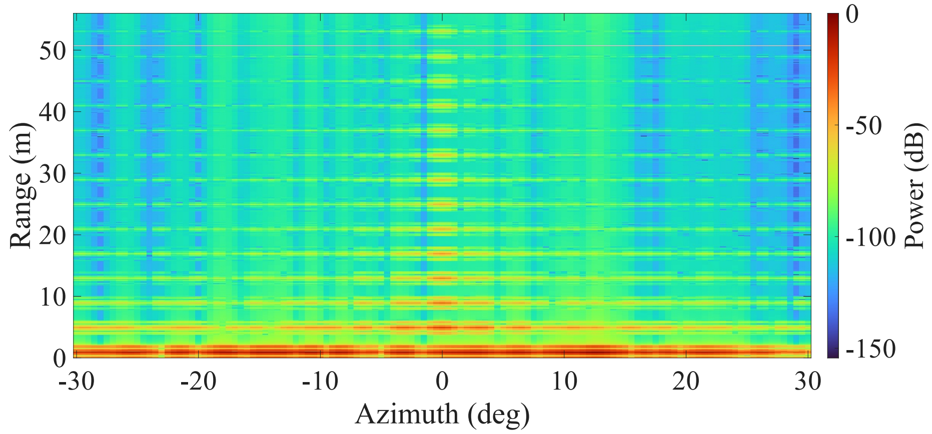

(a). Range-azimuth map normalized to the maximum return

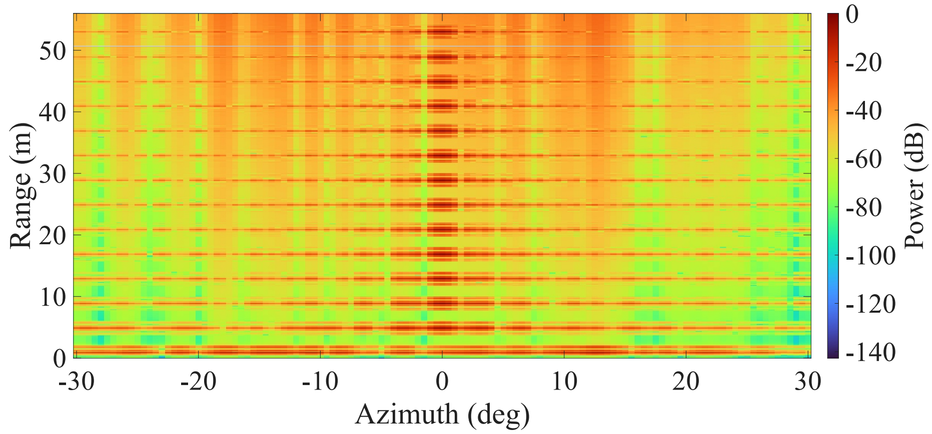

(b). Range-azimuth map with range-adjusted signal

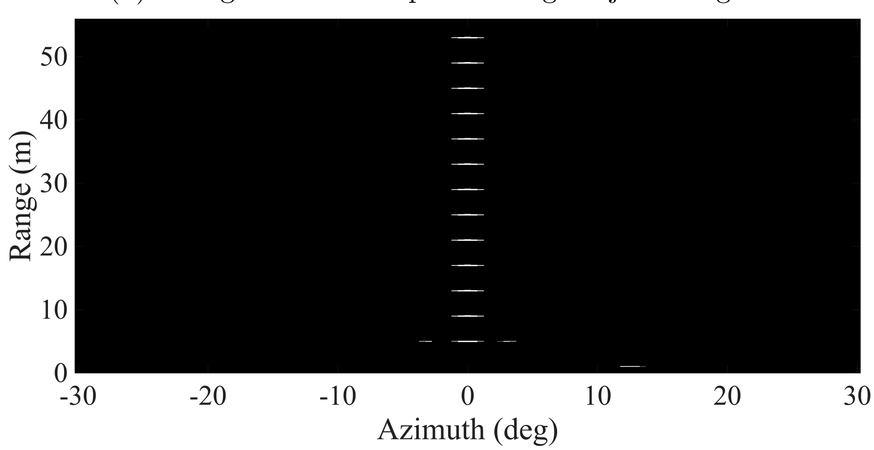

(c). Range-azimuth map with threshold detection

Figure 5.4: Range-azimuth maps showing the stages of threshold detection using 15 scatterers spaced 4 meters apart along 0° azimuth and processed with planar beamforming on a MIMO patch lattice

The dynamic range of the detection threshold logic is limited by the signal-to-noise ratio of the received echo. The range amplitude correction is applied in post-processing, so it increases the amplitude of noise in the more distant range bins as well as the signal echoes. To demonstrate this, Fig. 5.5 was generated with the same 15 targets and the same waveform used for Fig. 5.2, but with a receiver noise figure of 90 dB instead of 2.5 dB. Noise starts to exceed the threshold at about 30 meters and becomes increasingly prevalent in the range-azimuth map to the point that it completely washes out the target reflections as the range approaches 60 meters. A preferred result would be missed targets rather than false targets on the display. A constant false alarm rate (CFAR) approach to target detection would produce that result, and it would require the sidelobes of the close targets and the distant targets to be below the noise floor. With peak sidelobe levels of -11 dB, a noise floor above the peak sidelobes would limit the maximum range to 3.5 m for a system designed to detect targets at a minimum range of 1.0 m. A system that only needs to detect close targets, or a system designed to mitigate sidelobe levels, could use CFAR detection methods.

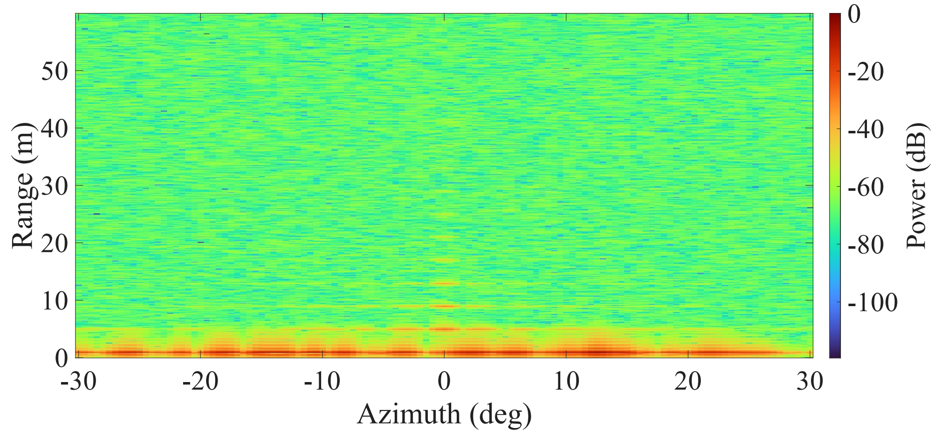

(a). Range-azimuth map normalized to the maximum return

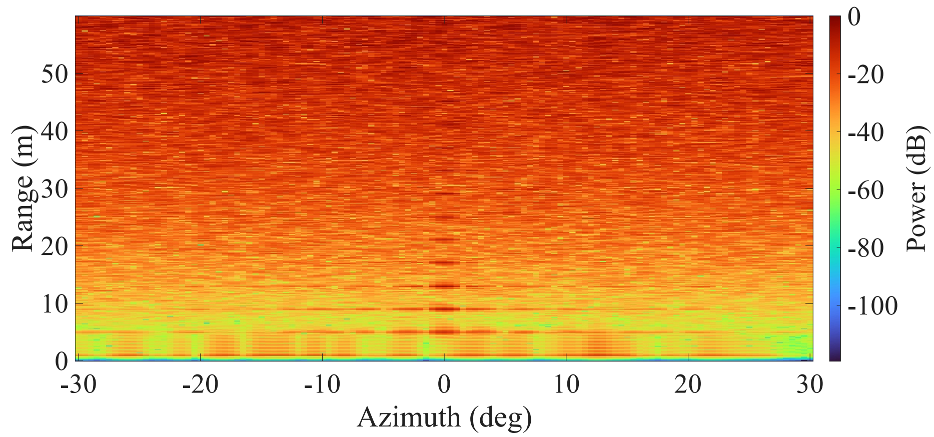

(b). Range-azimuth map with range-adjusted signal

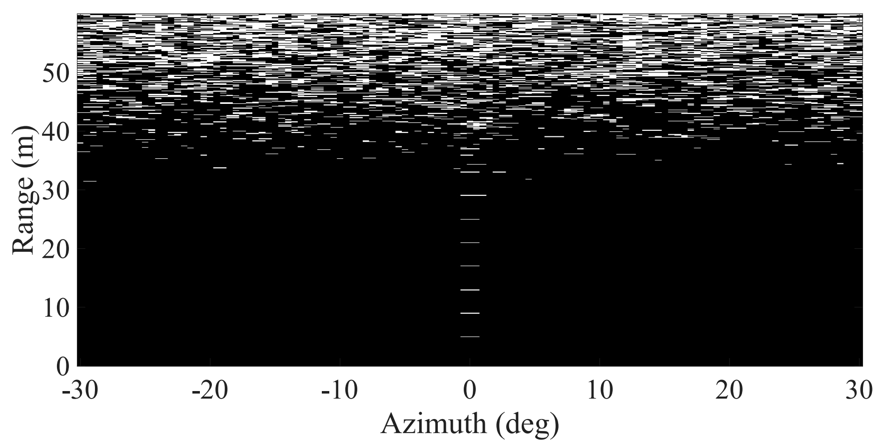

(c). Range-azimuth map with threshold detection

Figure 5.5: Range-azimuth maps showing the stages of threshold detection using 15 scatterers spaced 4 meters apart along 0° azimuth and processed with planar beamforming with a high noise floor

5.2 Range-Doppler Processing

A propagation environment with moving targets was set up to demonstrate the range-Doppler processing performance of this simulation. The same MIMO lattice as shown in Fig. 2.1 was used. A short-pulse LFM waveform, 7.5 ns wide with a 1 GHz bandwidth, is implemented to demonstrate the moving-target environment. The dwell has 33 pulses with a pulse repetition frequency of 5 kHz. Table 5.1 shows the location and range-rate of each of the targets. Fig. 5.6 shows the range-azimuth map of the target environment following the same threshold detection logic described in 4. The returns from target 3 are almost 25 dB higher than those from the other targets after flattening the range response, because it is the only target with 0 range rate. The lack of coherence between pulses and the range-bin migration of moving targets allows the stationary target to wash out the moving targets' returns in the detection logic.

Fig. 5.7 shows the range-Doppler map normalized to the maximum return and with threshold detection logic applied. The range sidelobes persist across the entire pulse width, which drove the need for a short pulse. As with the range-azimuth map, the non-moving target has the strongest range-adjusted return; however, the strength of the pulse-to-pulse coherence does not contribute to that difference on this map. The range-rate only affects the strength of the target return due to range bin migration, which is a much smaller effect.

	Range	Azimuth	Range-rate
1	1	-10	5
2	5	5	-5
3	10	5	0
4	15	-5	-10
5	20	0	10

Table 5.1: Moving target parameters

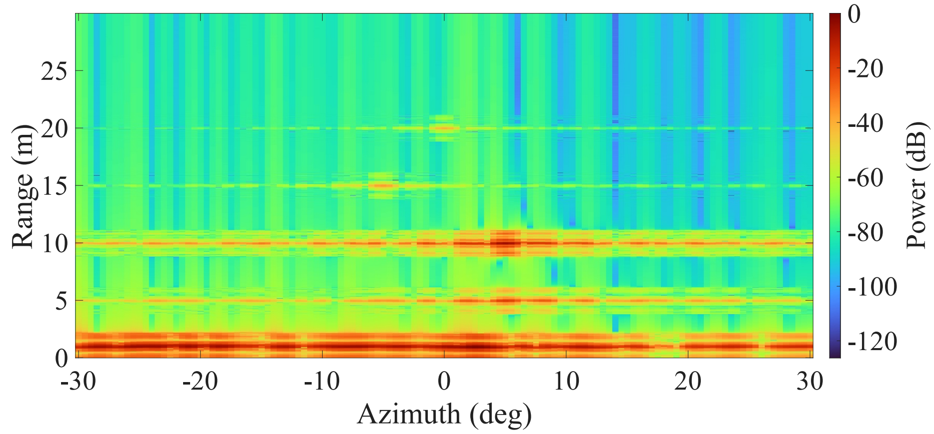

(a). Range-azimuth map normalized to the maximum return with 15 targets spaced 4 meters apart along 0° azimuth

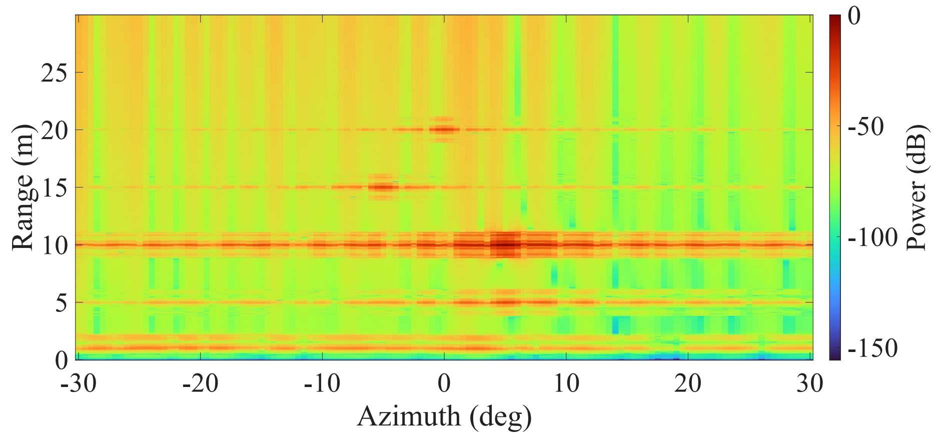

(b). Range-azimuth map with range adjusted signal

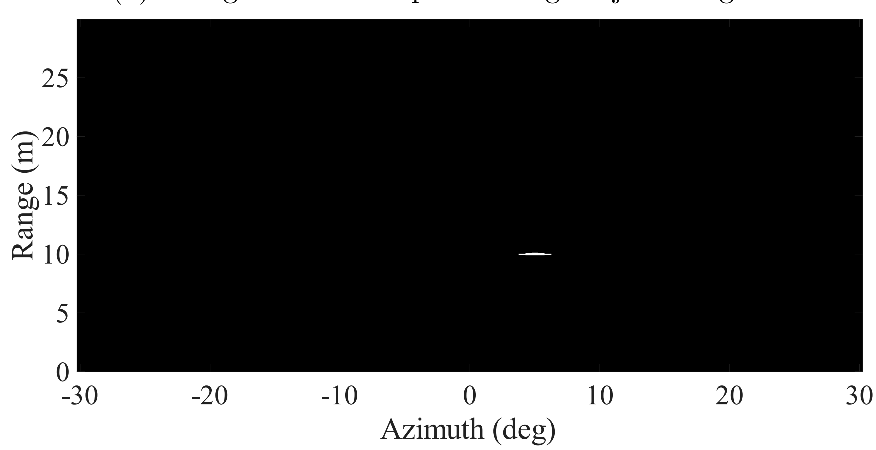

(c). Range-azimuth map with threshold detection

Figure 5.6: Range-azimuth maps showing the stages of threshold detection with scatterers arranged according to Table 5.1 and processed with planar beamforming

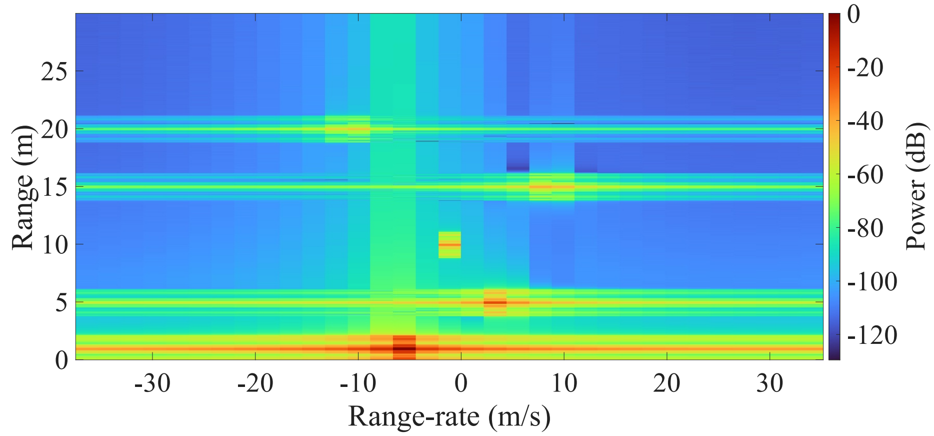

(a). Range-Doppler map normalized to the maximum return with 15 targets spaced 4 meters apart along 0° azimuth

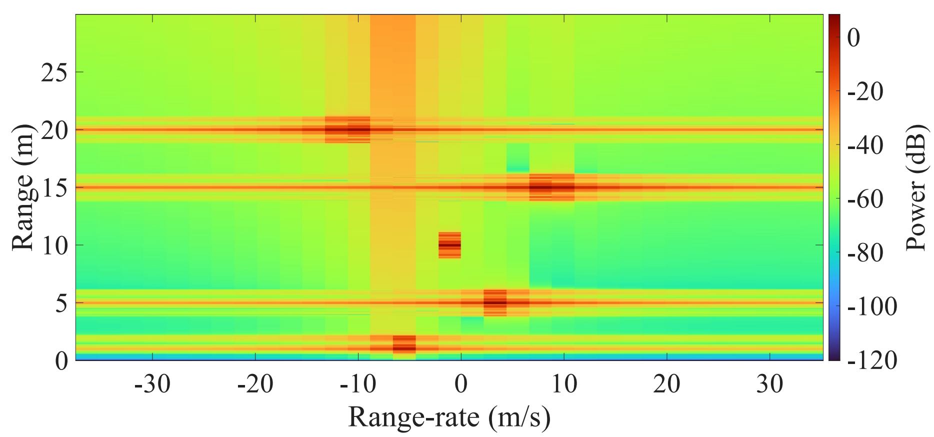

(b). Range-Doppler map with range-adjusted signal

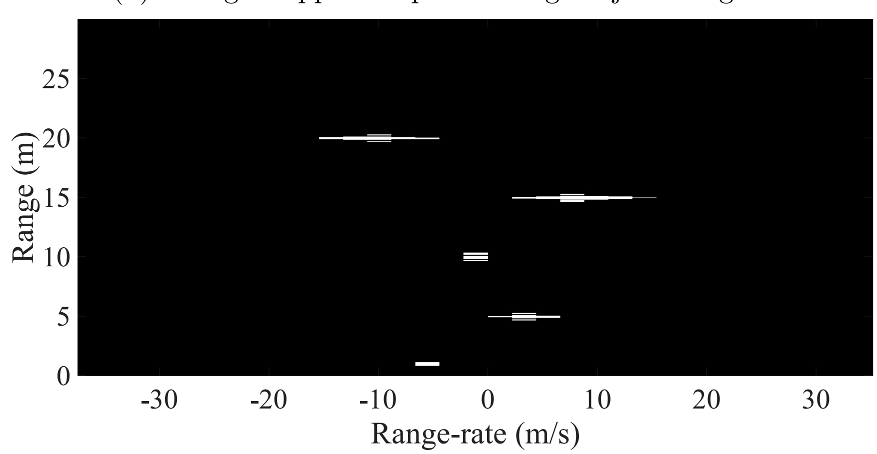

(c). Range-Doppler map with threshold detection

Figure 5.7: Range-Doppler maps showing the stages of threshold detection with scatterers arranged according to Table 5.1 and processed with planar beamforming

5.3 Spherical Beamforming

Fig. 5.9 is generated using the same waveform and propagation environment as was used for Fig. 5.2, but using the spherical beamforming method. In Fig. 5.8(a) we see that the first target is much more focused. The detection logic in Fig.5.8(b) correctly places the first target and does not pick up the sidelobes of the second target, demonstrating a clear improvement over the planar beamforming method.

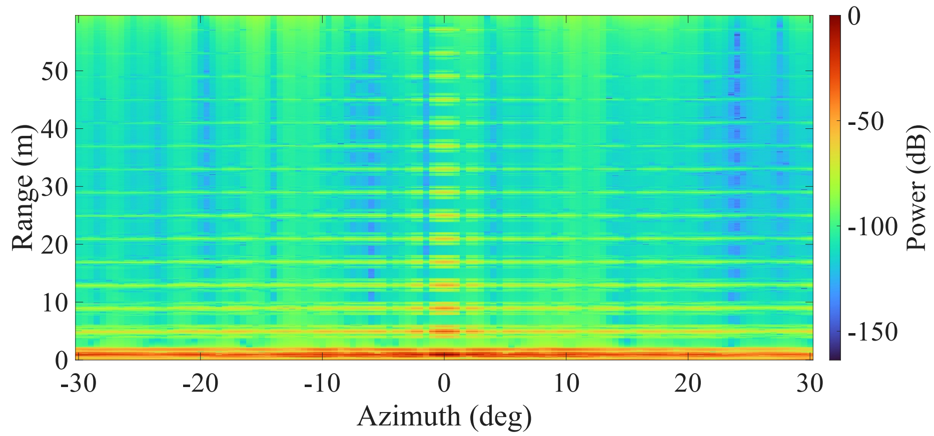

(a). Range-azimuth map normalized to the maximum return with 15 targets spaced 4 meters apart along 0° azimuth

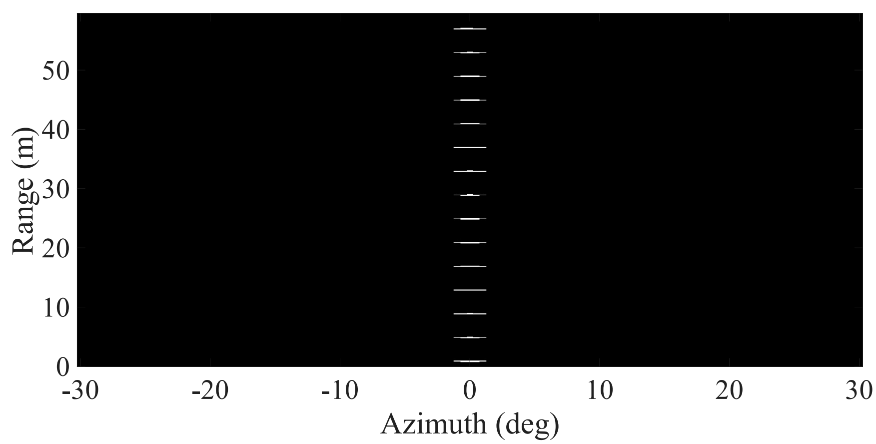

(b). Range-azimuth map with threshold detection

Figure 5.8: Range-azimuth maps showing the stages of threshold detection using 15 scatterers spaced 4 meters apart along 0° azimuth and processed with spherical beamforming

Fig. 5.9-5.10 were generated using the propagation environment described in table 5.1 with spherical beamforming. Fig. 5.9(a) shows improved focus, particularly on the first scatterer, that improvement is insufficient to show up in the detection logic. The improved focus is much more apparent on the range-Doppler maps shown in Fig. 5.10. The scatterers shown after applying threshold detection are narrower in the range and range-rate dimensions due to the improved focus of the spherical beamforming method.

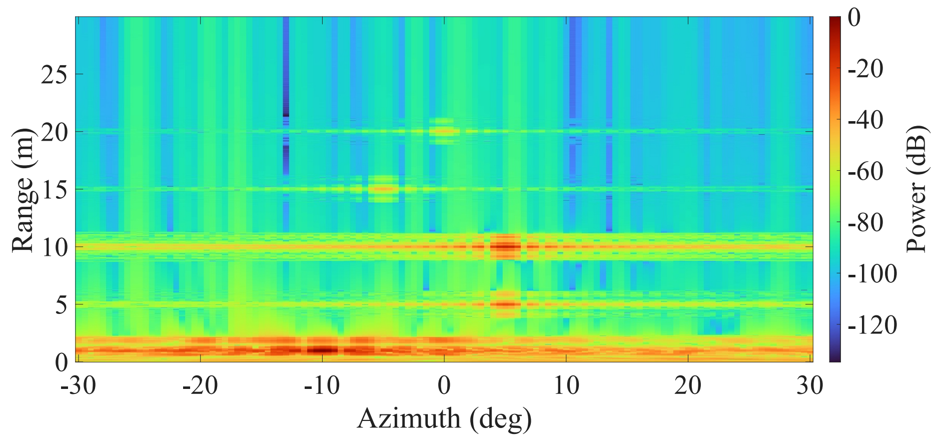

(a). Range-azimuth map normalized to the maximum return with 15 targets spaced 4 meters apart along 0° azimuth

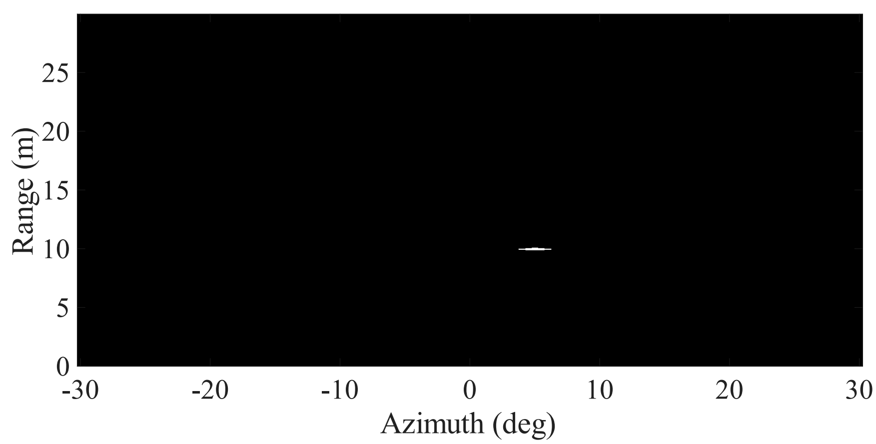

(b). Range-azimuth map with threshold detection

Figure 5.9: Range-azimuth maps showing the stages of threshold detection with scatterers arranged according to Table 5.1 and processed with spherical beamforming

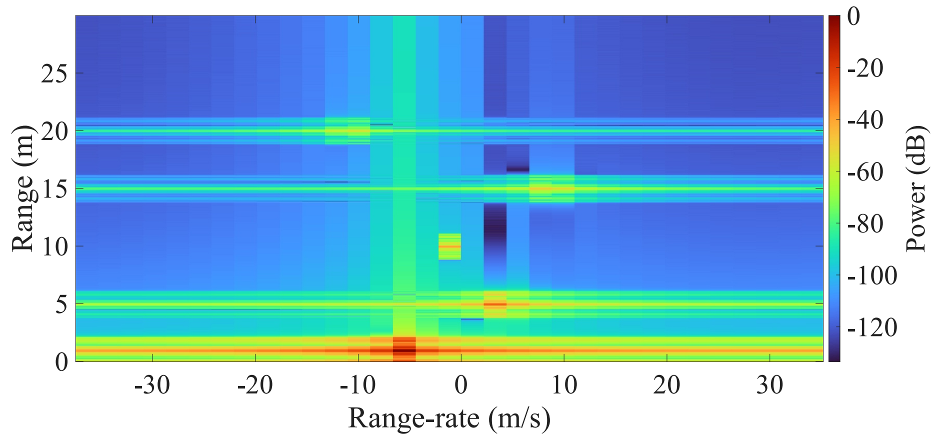

(a). Range-Doppler map normalized to the maximum return with 15 targets spaced 4 meters apart along 0° azimuth

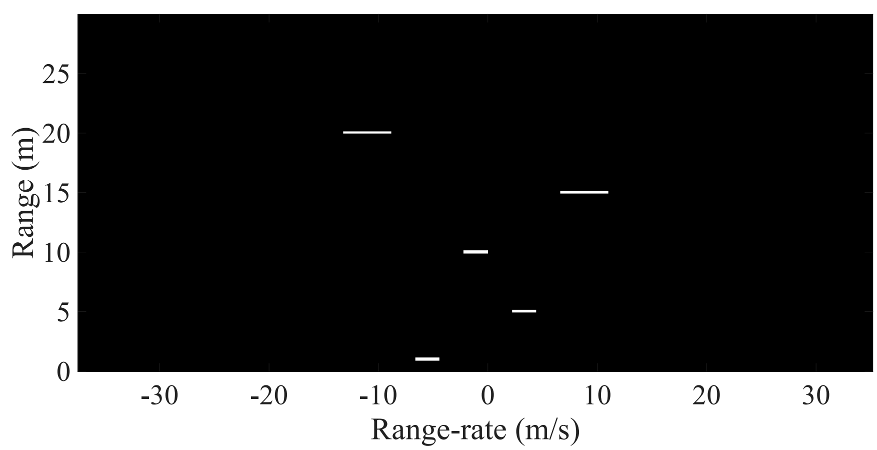

(b). Range-Doppler map with threshold detection

Figure 5.10: Range-Doppler maps showing the stages of threshold detection with scatterers arranged according to Table 5.1 and processed with spherical beamforming

5.4 Sidelobe Levels

To further explore the advantages of spherical beamforming, we set up a simulation that looped through the 15 targets shown in Fig. 5.2 one at a time and measured the sidelobe levels. For each target, we formed range-azimuth maps using planar and spherical beamforming and calculated the peak and integrated sidelobes for each. The targets were simulated one at a time to prevent sidelobes from nearby targets from interfering with the sidelobe-level calculations.

A one-dimensional slice of the range-azimuth map corresponding to the scatterer's range is sent to the sidelobe-level function, along with a value representing the noise floor of the signal. The sidelobe level calculation first finds the indices corresponding to peaks in the array and identifies the strongest peak as the center of the mainlobe. The peak sidelobe level is defined as the ratio of the magnitude of the mainlobe to the magnitude of the highest sidelobe expressed mathematically as

$$SLL_{peak} = -20 \log_{10} \left(\frac{|MB|}{|SL_{peak}|} \right) \tag{5.1}$$

where $|MB|$ is the magnitude of the main beam peak and $|SL_{peak}|$ is the magnitude fo the highest sidelobe peak. The integrated sidelobe is defined as the ratio of the mainlobe power to the total sidelobe power. The total sidelobe power is calculated by summing the squares of the magnitudes at each sidelobe index that falls within a sidelobe. The integrated sidelobe level can be expressed as

$$SLL_{integrated} = -10 \log_{10} \left(\frac{\sum_{l=1}^{N_{ML}} |ML_l|^2}{\sum_{m=1}^{N_{SL}} |SL_m|^2} \right) \tag{5.2}$$

where ML_l represents array indices that fall within the main lobe and SL_m represents array indices that fall within the sidelobes.

Fig. 5.11 shows the sidelobe levels for each target used to generate Fig. 5.2, simulated one at a time using both the planar and spherical beamforming methods. As expected, the spherical method shows the greatest improvement over the planar method for targets very near the MIMO lattice. As the target range increases, the sidelobe levels corresponding to the planar method converge to the sidelobe levels corresponding to the spherical method. The MIMO lattice studied in this paper is 1.17 meters in length. As the target range increases beyond 10 times the array size, the difference in peak sidelobe levels converges quickly, although there is still a slight benefit to using the spherical method even at 60 meters. Fig. 5.12 shows single range bin slices at $r' = 1$ meter and $r' = 57$ meters from the data set used to generate the sidelobe level comparison in Fig. 5.11.

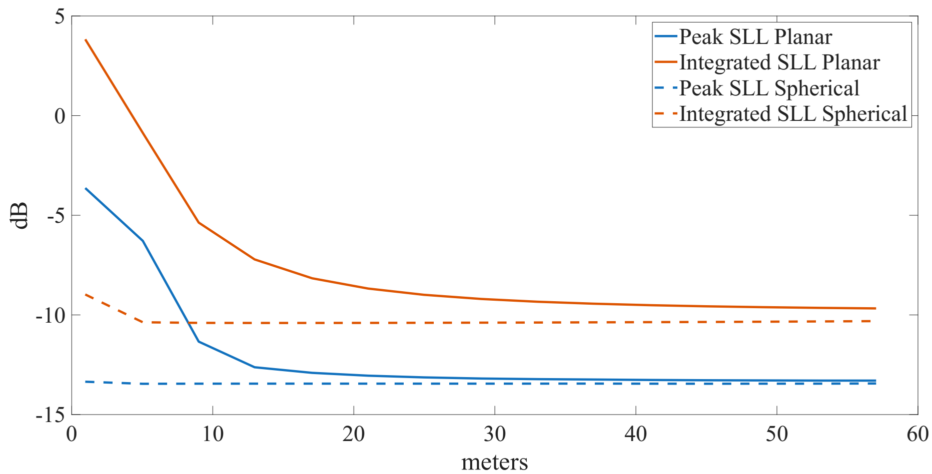

Figure 5.11: Comparison of integrated and peak sidelobe levels between planar and spherical beamforming methods for scatterers positioned along 0° azimuth and positioned every 4 meters starting at 1 meter.

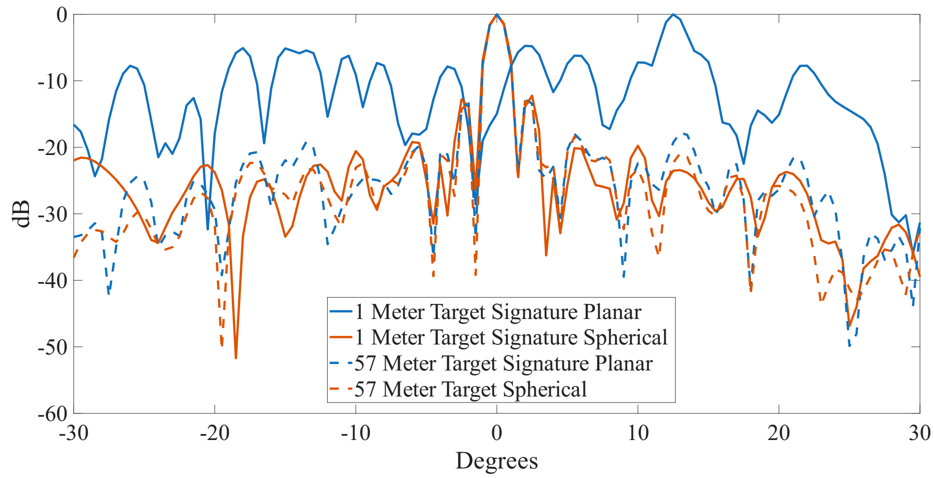

Figure 5.12: Comparison of power magnitude vs. azimuth for range bins $r = 1$ meter and $r = 57$ meters using planar and spherical beamforming methods with targets along the $\phi' = 0^{\circ}$ look angle.

Fig. 5.13 - 5.14 show sidelobe levels for simulations executed with the same pattern used for Fig. 5.11 but with scatterers arranged along 5° and -25° azimuth angles and their corresponding range-azimuth maps simulated with all targets present simultaneously. At 5° off boresight, the peak sidelobe level is approximately -8 dB, which is worse than at 0° and -25°. To properly set the threshold, the peak sidelobe levels would need to be calculated for every look angle, and the worst case would be used as the threshold to prevent sidelobes from generating false detections. It is also worth noting that the main beam forms two peaks for targets -25° off boresight using planar beamforming, while having a single narrow peak using spherical beamforming. This shows that spherical beamforming could increase the maximum usable steering angle for distant targets at the cost of increased computational resources. Fig. 5.15 - 5.16 show single range bin slices of the data used to generate Fig. 5.13- 5.14, comparing target signatures for spherical and planar beamforming methods at $r' = 1$ and $r' = 57$ meters.

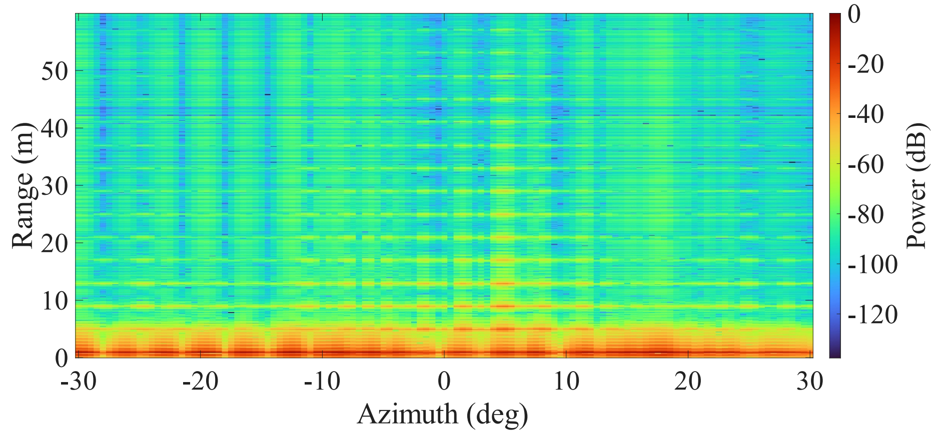

(a). Planar beamforming normalized to the maximum return

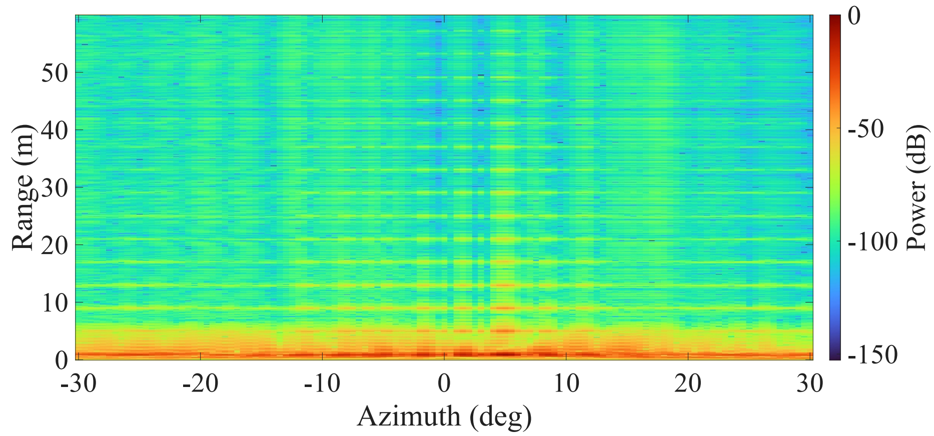

(b). Spherical beamforming normalized to the maximum return

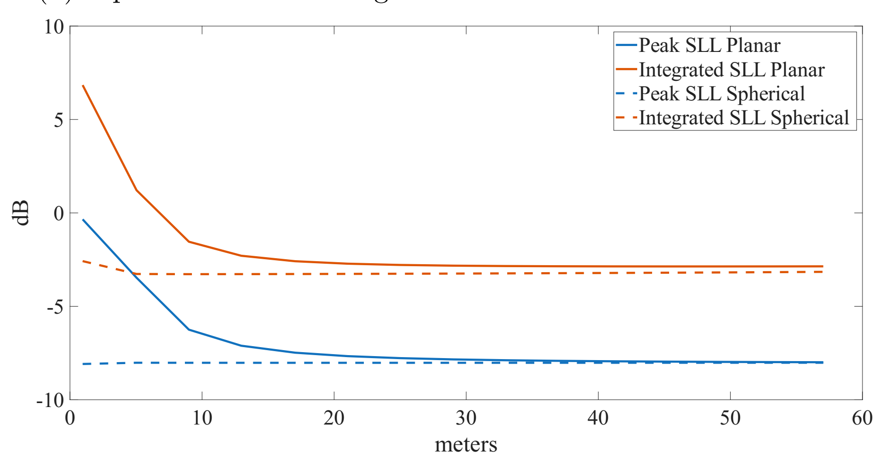

(c). Integrated and peak sidelobe levels from planar and spherical beamforming methods

Figure 5.13: Comparison of planar and spherical beamforming methods using 15 targets spaced 4 meters apart along 5° azimuth

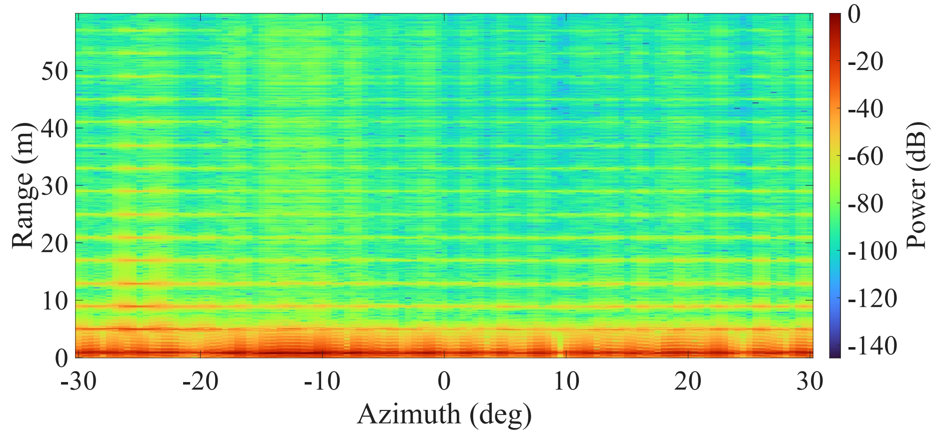

(a). Planar beamforming normalized to the maximum return

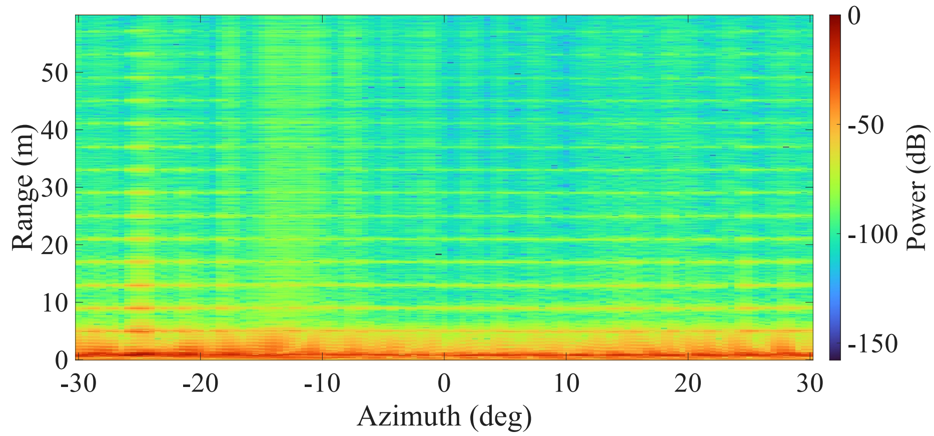

(b). Spherical beamforming normalized to the maximum return

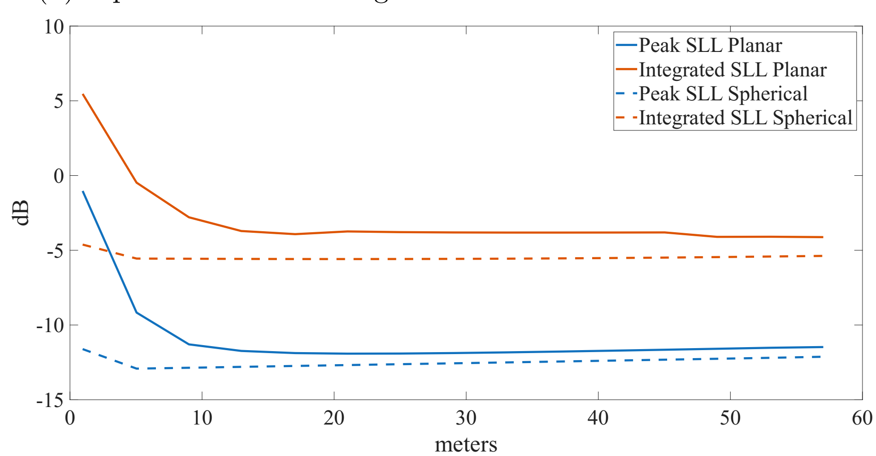

(c). Integrated and peak sidelobe levels from planar and spherical beamforming methods

Figure 5.14: Comparison of planar and spherical beamforming methods using 15 targets spaced 4 meters apart along -25° azimuth

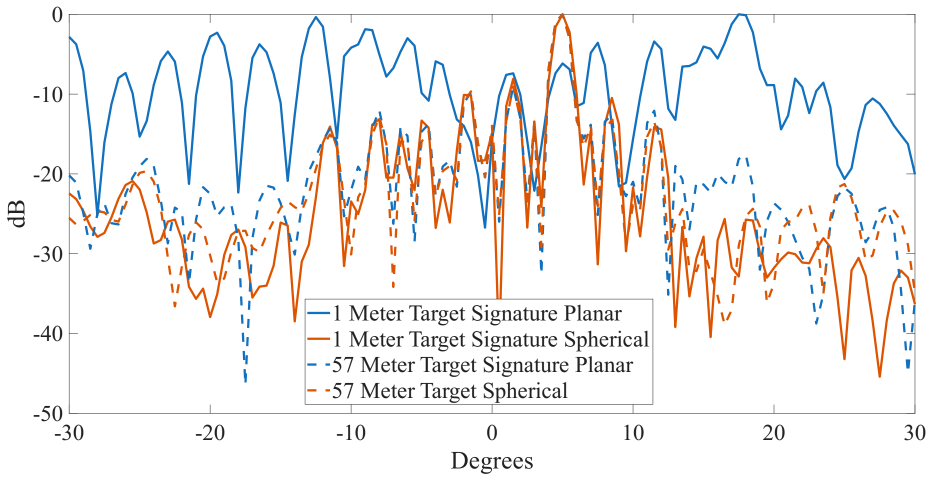

Figure 5.15: Comparison of power magnitude vs. azimuth for range bins $r = 1$ meter and $r = 57$ meters using planar and spherical beamforming methods with targets along the $\phi' = 5^\circ$ look angle.

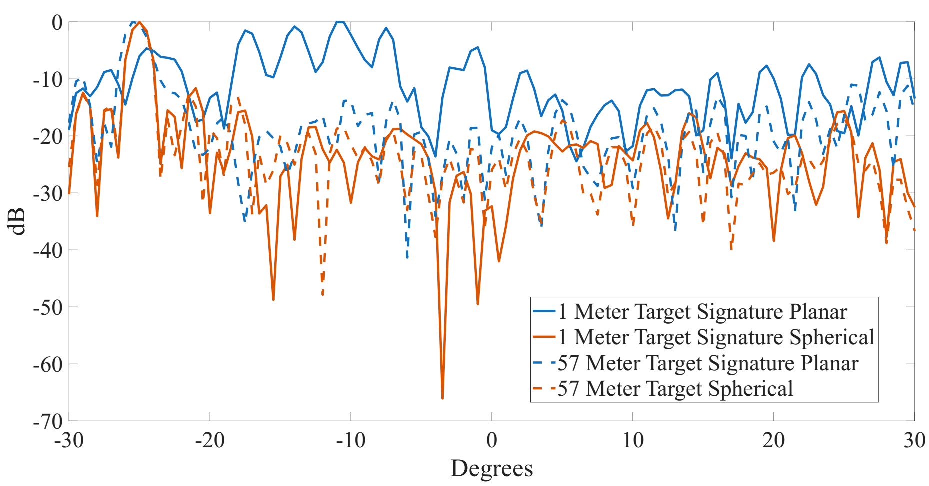

Figure 5.16: Comparison of power magnitude vs. azimuth for range bins $r = 1$ meter and $r = 57$ meters using planar and spherical beamforming methods with targets along the $\phi' = -25^\circ$ look angle.

Table 5.2 summarizes the difference in sidelobe levels between planar beamforming and spherical beamforming for the three stationary target scenarios described above. The four meter range is the nearest target selected for the summary table because it is the first target that is correctly located by the planar beamforming algorithm. The

13 meter range is selected because it is knee of the curve as the results of the planar and spherical beamforming methods begin to converge. The 49 meter range is shown because it is well past where the improvement shown for spherical beamforming levels out.

	0° Azimuth			5° Azimuth			-25° Azimuth		
	5m	13m	49m	5m	13m	49m	5m	13m	49m
Peak SLL	4.7	0.57	0.19	4.55	0.91	0.05	3.75	1.07	0.67
Integrated SLL	7.92	2.46	0.54	4.48	0.98	0.32	5.08	1.87	1.35

Table 5.2: Summary of sidelobe level improvement in decibels of spherical beamforming over planar beamforming

Chapter 6

Conclusion and Future Work

6.1 Summary of Contributions

This work developed an analytical framework for studying close-range target detection and localization in MIMO radar. A digital beamforming algorithm was proposed to focus energy from close-range targets. Perhaps more importantly, a simulation environment was developed to test the beamforming algorithm and other aspects of the MIMO radar system. The simulation environment can model the MIMO target returns of moving objects, and its parameters can be easily adapted to emulate a developmental radar system. The simulation environment includes a waveform generator, a transmitter, a MIMO antenna lattice, a receiver, and a post-processor. The simulation is shown to perform near- and far-target detection in range-azimuth and range-Doppler. The adaptability of the simulation environment can be leveraged to aid in selecting MIMO system components and to test algorithms that support any desired radar mode.

6.2 Future Work

The simulation environment presented in this work can be improved in various ways to enhance realism and to explore other topics related to MIMO radar performance. If a MIMO lattice design were under consideration for a radar system, it could be simulated in a computational electromagnetics environment to determine the antenna patterns of the individual elements and the mutual coupling between them. The MIMO simulation environment already incorporates a closed-form mutual coupling model of a half-wavelength dipole. A mutual coupling model derived from computational electromagnetics could be easily incorporated to yield a more realistic system model.

This work took a naive approach to waveform orthogonality, which is essential for any MIMO system. A real MIMO radar system would require a fully developed waveform scheme with full, or at least partial, waveform orthogonality among the transmitters. That waveform scheme could be incorporated into this schematic, eliminating the need to track transmit/receive pairs in the propagation environment and instead combining the signals at each receiver with the appropriate amplitude and phase modulations for each scatterer. The transmit/receive pairs would then be identified by matched filtering. This would enable analysis of different waveform schemes and allow the system designer to conduct a trade-off analysis based on the overall system requirements before incurring the time and expense of fabricating a prototype. Range sidelobes could be improved by implementing sidelobe-ratio filters [27]. A natural extension of the implementation of waveform diversity in the MIMO system simulation would be the incorporation of frequency diversity. A frequency diverse MIMO array provides additional degrees of freedom in range-angle control for adaptive beamforming, sidelobe suppression, and interference suppression [28, 29]. The peak sidelobe levels of the MIMO array are a significant limiting factor for the dynamic range, both in terms of target RCS and target distance. Implementing sidelobe-reduction techniques such as array tapers and windowing functions, along with careful waveform selection, would greatly improve the flexibility of the MIMO radar system. This simulation environment could be a useful tool for evaluating various sidelobe reduction methods against system performance requirements [30].

This work focused entirely on pulsed-Doppler processing. Many MIMO systems, particularly those used for near-range sensing, employ frequency-modulated continuous-wave (FMCW) processing. Adding FMCW capability to this simulation would greatly enhance its usefulness and flexibility. Many adaptive beamforming and target detection techniques could be implemented and tested in this simulation framework to improve overall system performance [31]. Some of those techniques include the robust Capon beamforming [32], amplitude and phase estimation filtering (APES) [33], and Capon-APES [34]. Also, this simulation assumed all scatterers were point targets that had the same RCS from every look angle. A higher fidelity simulation would include statistical RCS from the targets that vary randomly for each look angle, particularly for close range targets. Finally, this work assumed perfect lossless matching in the microwave networks internal to the MIMO radar system. A real system with defined S-parameters at the component interfaces could be implemented in this simulation as part of the mutual coupling calculation. Including internal system S-parameters would improve the realism of the simulation and provide an opportunity to optimize any matching networks included in the system design before prototyping [20].

References

[1] S. Sun, A. P. Petropulu, and H. V. Poor, "Mimo radar for advanced driver-assistance systems and autonomous driving: Advantages and challenges," *IEEE Signal Processing Magazine*, vol. 37, no. 4, pp. 98–117, 2020.

[2] Y. Tao, Z. Gao, Z. Li, Z. Wan, T. Li, C. Zhu, L. Chen, G. Wen, D. Zheng, and D. Niyato, "Pseudo-random tdm–mimo fmcw-based millimeter-wave sensing and communication integration for uav swarm," *IEEE Internet of Things Journal*, vol. 13, no. 1, pp. 549–564, 2026.

[3] S. M. Patole, M. Torlak, D. Wang, and M. Ali, "Automotive radars: A review of signal processing techniques," *IEEE Signal Processing Magazine*, vol. 34, no. 2, pp. 22–35, 2017.

[4] G. Rankin, A. Tirkel, and A. Leukhin, "Millimeter wave array for uav imaging mimo radar," in *2015 16th International Radar Symposium (IRS)*, 2015, pp. 499–504.

[5] E. Fishler, A. Haimovich, R. Blum, D. Chizhik, L. Cimini, and R. Valenzuela, "Mimo radar: an idea whose time has come," in *Proceedings of the 2004 IEEE Radar Conference (IEEE Cat. No.04CH37509)*, 2004, pp. 71–78.

[6] A. Hassanien and S. A. Vorobyov, "Phased-mimo radar: A tradeoff between phased-array and mimo radars," *IEEE Transactions on Signal Processing*, vol. 58, no. 6, pp. 3137–3151, 2010.

[7] J. Yu and J. Krolik, "Mimo multipath clutter mitigation for gmti automotive radar in urban environments," in *IET International Conference on Radar Systems (Radar 2012)*, 2012, pp. 1–5.

[8] S. Fortunati, L. Sanguinetti, F. Gini, M. S. Greco, and B. Himed, "Massive mimo radar for target detection," *IEEE Transactions on Signal Processing*, vol. 68, pp. 859–871, 2020.

[9] H. Wang, Z. Xiao, and Y. Zeng, "Cramér-rao bounds for near-field sensing with extremely large-scale mimo," *IEEE Transactions on Signal Processing*, vol. 72, pp. 701–717, 2024.

[10] X. Zhuge and A. G. Yarovoy, "Three-dimensional near-field mimo array imaging using range migration techniques," *IEEE Transactions on Image Processing*, vol. 21, no. 6, pp. 3026–3033, 2012.

[11] Z. Hu, T. Su, D. Xu, F. Gini, and M. S. Greco, "An efficient two-stage near-field 3-d imaging algorithm for massive mimo radar with range migration and admm," *IEEE Transactions on Antennas and Propagation*, vol. 74, no. 4, pp. 3440–3455, 2026.

[12] S. Wu, C. Li, G. Yang, S. Zheng, H. Gao, H. Geng, M. Zhao, X. Liu, and G. Fang, "Terahertz 3-d imaging for non-cooperative on-the-move whole body by scanning mimo-array-based gaussian fan-beam," *IEEE Transactions on Antennas and Propagation*, vol. 70, no. 12, pp. 12 147–12 162, 2022.

[13] K. Tan and X. Chen, "Precise near-range 3-d image reconstruction based on mimo circular synthetic aperture radar," *IEEE Transactions on Microwave Theory and Techniques*, vol. 69, no. 5, pp. 2651–2661, 2021.

[14] E. Kim, I. Kim, and W. Kim, "Non-uniform mimo array design for radar systems using multi-channel transceivers," *Remote Sensing*, vol. 15, no. 1, January 2023.

[15] C. A. Balanis, *Antenna Theory*, 4th ed. Hoboken, NJ, USA: John Wiley & Sons, Inc., 2016.

[16] E. Grosicki, "A weighted linear prediction method for near-field source localization," *IEEE Transactions on Geoscience and Remote Sensing*, vol. 36, no. 5, pp. 1578–1588, 1998.

[17] Y. Yang and R. S. Blum, "Minimax robust mimo radar waveform design," *IEEE Journal of Selected Topics in Signal Processing*, vol. 1, no. 1, pp. 147–155, June 2007.

[18] D. J. Rabideau, "Mimo radar waveforms and cancellation ratio," *IEEE Transactions on Aerospace and Electronic Systems*, vol. 48, no. 2, pp. 1167–1178, April 2012.

[19] X. Du, S. Zhou, and M. Zhang, "A sub-array mimo radar waveform design with wide pulse compression main-lobe," in *IEEE Internation Radar conference*. IEEE, 2023.

[20] B. T. Arnold, "The effects of antenna coupling in a mimo radar system," Master's thesis, Brigham Young University, 2016.

[21] U. Majumder, M. R. Bell, and M. Rangaswamy, "Design and analysis of radar waveforms achieving transmit and receive orthogonality," *IEEE Transactions on Aerospace and Electronic Systems*, vol. 52, no. 3, pp. 1056–1066, 2016.

[22] K. Zhong, J. Hu, Z. Zhao, X. Yu, G. Cui, B. Liao, and H. Hu, "Mimo radar unimodular waveform design with learned complex circle manifold network," *IEEE Transactions on Aerospace and Electronic Systems*, vol. 60, no. 2, pp. 1798–1807, 2024.

[23] G. Chang, A. Liu, C. Yu, Y. Ji, Y. Wang, and J. Zhang, "Orthogonal waveform with multiple diversities for mimo radar," *IEEE Sensors Journal*, vol. 18, no. 11, pp. 4462–4476, 2018.

[24] M. L. Skolnik, *Introduction to Radar Systems*, 3rd ed. New York, NY, USA: McGraw Hill, 2001.

[25] H. Rohling, "Radar cfar thresholding in clutter and multiple target situations," *IEEE transactions on aerospace and electronic systems*, no. 4, pp. 608–621, 2007.

[26] ——, "Ordered statistic cfar technique - an overview," in *2011 12th International Radar Symposium (IRS)*, 2011, pp. 631–638.

[27] M. S. Davis and A. D. Lanterman, "Minimum integrated sidelobe ratio filters for mimo radar," *IEEE Transactions on Aerospace and Electronic Systems*, vol. 51, no. 1, pp. 405–416, 2015.

[28] W. Xu, Z. Deng, P. Huang, W. Tan, and Z. Gao, "Beampattern synthesis and optimization for frequency diverse arc array based on the virtual element," *Electronics*, vol. 12, no. 10, 2023. [Online]. Available: https://www.mdpi.com/2079-9292/12/10/2231

[29] J. Cheng, M. Juhlin, A. Jakobsson, and W.-Q. Wang, "Designing optimal frequency offsets for frequency diverse array mimo radar," *IEEE Transactions on Aerospace and Electronic Systems*, vol. 59, no. 6, pp. 8104–8118, 2023.

[30] H. A. Diawuo, S. J. Lee, and Y.-B. Jung, "Sidelobe-level reduction of a linear array using two amplitude tapering techniques," *IET Microwaves, Antennas & Propagation*, vol. 11, no. 10, pp. 1432–1437, 2017. [Online]. Available: https://ietresearch.onlinelibrary.wiley.com/doi/abs/10.1049/iet-map.2016.0883

[31] L. Xu, J. Li, and P. Stoica, "Adaptive techniques for mimo radar," in *Fourth IEEE Workshop on Sensor Array and Multichannel Processing, 2006.*, 2006, pp. 258–262.

[32] P. Stoica, Z. Wang, and J. Li, "Robust capon beamforming," *IEEE Signal Processing Letters*, vol. 10, no. 6, pp. 172–175, 2003.

[33] P. Stoica, H. Li, and J. Li, "A new derivation of the apes filter," *IEEE Signal Processing Letters*, vol. 6, no. 8, pp. 205–206, 1999.

[34] A. Jakobsson and P. Stoica, "Combining capon and apes for estimation of spectral lines," *Circuits, Systems and Signal Processing*, vol. 19, no. 2, pp. 159–169, 2000.

Appendix A - List Of Symbols

$\mathbf{a_{nr}}$	Standard normal distribution of random real numbers from 0 to 1
$j\mathbf{a_{ni}}$	Standard normal distribution of random imaginary numbers from j0 to j1
$\mathbf{\hat{a}_r}$	Radial unit vector
$\mathbf{\hat{a}_theta}$	Polar unit vector
$\mathbf{\hat{a}_phi}$	Azimuthal unit vector
$\mathbf{\hat{a}_x}$	Unit vector pointing in the $+x$ direction of the cartesian coordinate system
$\mathbf{\hat{a}_y}$	Unit vector pointing in the $+y$ direction of the cartesian coordinate system
$\mathbf{\hat{a}_z}$	Unit vector pointing in the $+z$ direction of the cartesian coordinate system
Ci	Cosine integral
Cin	Even cosine integral
$\mathbf{D^{(R)}}$	linear operator transforming open-circuit voltage on the receive antennas to voltages on the loads
$\mathbf{D^{(T)}}$	linear operator transforming voltage on source to currents in the transmit antennas
e	Euler's number
e_{cd}	Combined conductive and dielectric antenna efficiency
E_r	Radial component of the electric field
E_θ	Polar component of the electric field
E_ϕ	Azimuthal component of the electric field
$\mathbf{E}$	Electric field vector

f_0	Center frequency
F_{adc}	Sampling rate of analog-to-digital converter in Hz
F_n	linear noise figure
G	Gain
H_r	Radial component of the magnetic field
H_θ	Polar component of the magnetic field
H_ϕ	Azimuthal component of the magnetic field
$\mathbf{H}$	Magnetic field vector
I_0	Current on the antenna
I_e	Current distribution on the antenna
j	Imaginary number equal to $\sqrt{-1}$
k	Wavenumber as the ratio of 2π to the wavelength
l	Length in meters
$\mathbf{L_{pulse}}$	Number of samples in a pulse
$\mathbf{N_{out}}$	Noise output
P_{acc}	Power accepted by the antenna
P_{env}	Complex envelope of pulse
P_{rad}	Radiated power
r	Distance from the origin
$\Re$	Real component of a complex value or function
$\mathbf{S}$	Matix of scattering parameters
$\mathbf{S_A^{(R)}}$	Scattering parameter matix of the receive antenna array
$\mathbf{S_A^{(T)}}$	Scattering parameter matix of the transmit antenna array
Si	Sine integral
T_0	Reference temperature
T_p	Pulse width in seconds

U	Radiation intensity
$\mathbf{v_{chirp}}$	chirp function
vp	Velocity of propagation
W_{av}	Magnitude of the power density vector
$\mathbf{W_{av}}$	Average power density vector
Z_0	Characteristic system impedance
$\mathbf{Z}$	Impedance parameter matrix
$alpha$	reflection coefficient
β	bandwidth
γ	Euler-Mascheroni constant
η	Impedance of the medium of propagation
λ	Wavelength in meters
π	Ratio of the circumference of a circle to its diameter
Σ	Sum
σ	Radar cross section
τ	Time delay in seconds
ϕ	Azimuthal angle
$(\cdot)^*$	Complex conjugate operator
$\bigotimes$	Convolution operator

Appendix B - List Of Acronyms and Abbreviations

APES	Amplitude and phase estimation
CFAR	Continuous False Alarm Rate
FMCW	Frequency Modulated Continuous Wave
LFM	Linear Frequency Modulated
LiDAR	Light Direction and Range
MIMO	Multi-Input Multi-Output
RCS	Radar Cross Section
STAP	Space-Time Adaptive Processing
STC	Sensitivity Time Control
SWaP	Size, Weight, and Power
UxV	Unmanned Vehicle